RSC Sustainability

ROYAL SOCIETY OF CHEMISTRY

PAPER

View Article Online
View Journal | View Issue

Cite this: *RSC Sustainability*, 2026, 4, 2288

Eichhornia crassipes-derived biochar *via* slow pyrolysis for the removal of Reactive Yellow 176 dye from aqueous media: adsorption isotherm, kinetic and thermodynamic studies

Nawshin Farzana,[ab] Rayhan Bin Masud,[a] Tahzib Rayhan Himadry [a] and Md. Shahinoor Islam *[a]

Biochars (300BC, 500BC, and 700BC) were produced from water hyacinth at pyrolysis temperatures of 300 °C, 500 °C, and 700 °C. The adsorption capacities were evaluated using Reactive Yellow 176 dye. Characterization of the resultant biochar was conducted using proximate analysis, ultimate analysis, SEM, EDX, XRD, FTIR, BET surface area, and TGA-DTG analysis. Increasing pyrolysis temperature enhanced pore formation and surface heterogeneity, facilitating the mass transfer of dye molecules. FTIR analysis indicated hierarchical aromaticity and graphitization with increasing temperature, complemented by the confirmation of carbonaceous structures in XRD analysis. The specific surface area of the biochar pyrolyzed at 700 °C (211.3 m^2 g^{-1}) increased nearly 59-fold and 7-fold compared to the 300 °C (3.6 m^2 g^{-1}) and 500 °C (30.9 m^2 g^{-1}) counterparts, promoting pore filling, electrostatic interactions and π–π interactions. Adsorption kinetics followed the pseudo-second-order model, while the equilibrium isotherm analysis revealed a perfect agreement with the Langmuir isotherm model (R^2 = 0.99 for each biochar species, low RMSE values from 0.23 to 0.39, and reduced χ^2 values ranging from 0.06 to 0.35), indicating monolayer adsorption on a homogeneous surface. The intraparticle diffusion model confirmed that the initial film diffusion was limited by the subsequent intraparticle diffusion. 700BC demonstrated the best dye adsorption capacity (19.68 mg g^{-1}) attributed to its microporous structure, elevated specific surface area (211.3 m^2 g^{-1}), highest point of zero charge (10.3), and highest aromaticity. The spontaneity and exothermic nature of the adsorption mechanism were validated using ΔG (−24.71 kJ mol^{-1} to −30.42 kJ mol^{-1}) and ΔH (−27.59 to −45.73 kJ mol^{-1}) values. The proposed adsorption pathway aligns with existing literature, suggesting that pore filling, electrostatic attractions, hydrophobic interactions, H–H bonding, ion exchange, and π–π interactions drive the adsorption mechanism. The study demonstrated that the water hyacinth-derived biochar can emerge as a sustainable and efficient adsorbent for reactive anionic dyes.

Received 11th December 2025
Accepted 23rd February 2026

DOI: 10.1039/d5su00918a

rsc.li/rscsus

Sustainability spotlight

The study exemplifies the principles of circular economy by addressing the removal of Reactive Yellow 176 from an aqueous medium using water hyacinth (*Eichhornia crassipes*) derived biochar. This research successfully established water hyacinth, an invasive plant species, as an eco- and cost-efficient precursor for effective adsorbent synthesis, thereby providing pathways for environmental remediation from an environmentally detrimental feedstock. The superior adsorption capacity of water hyacinth-derived biochars (up to 19.68 mg.g^{-1}), an excellent fit to the Langmuir isotherm, and thermodynamic spontaneity (negative values of ΔG and ΔH) indicate that the biochar is suitable for real-world applications. The integrated dual solution approach for controlling water hyacinth population and dye removal in this study provides a significant step for addressing such environmental challenges.

1 Introduction

The worldwide growth of the textile industry has led to a sharp increase in wastewater generation, comprising complex mixtures of diverse pollutants such as synthetic dyes, surfactants, auxiliary chemicals, salts, and various organic and inorganic substances. Among these contaminants, textile dyes are considered to be the most concerning issues due to their recalcitrant aromatic structures, toxicity, resistance to biodegradation, and visible color even in the presence of very diluted concentrations.[1] Being one of the world's leading exporters of cotton-based apparel, Bangladesh has experienced dramatic

[a]*Department of Chemical Engineering, Bangladesh University of Engineering and Technology, Dhaka-1000, Bangladesh. E-mail: shahinoorislam@che.buet.ac.bd*
[b]*Ahsanullah University of Science and Technology, Dhaka-1208, Bangladesh*

expansion in the textile dyeing, finishing, washing, and printing industries. This has intensified the discharge of untreated or partially treated dye-containing effluents into nearby rivers, lakes, and canals.[2] The industries, particularly the wet processing sectors, highly rely on reactive dyes for the dyeing and printing of cotton and cotton-blended materials due to their bright shades, high color fastness properties, ease of application, and versatility.[3] According to previous literature, dyeing 1 kg of cotton can produce 200 kg of wastewater, which can contain up to 50% of the dyebath's initial dye input and up to 100 g L^{-1} of salts.[4] However, a major limitation of using reactive dyes is the limited fixation percentage (typically only about 50–85%) to the fiber, due to hydrolysis during wet processing, particularly dyeing. The remaining 15–50% unfixed dyes undergo post-dyeing rinsing treatments and get into the wash-off liquor.[5] These dyes, typically containing aromatic amines in their structure, can decompose into mutagenic and carcinogenic metabolites in discharged water bodies.[6] Moreover, this fraction of unfixed dyes significantly contributes to the pollution load of textile effluents by increasing chemical oxygen demand and color intensity, odour and turbidity[7] and may further aggravate toxicity by persisting in the aquatic environment due to being highly soluble in water and containing potentially hazardous intermediates, leading to disruption of the microbial ecosystem.[8,9]

Numerous effluent treatment strategies have been explored in the literature to date for the abatement of dye pollutants from textile effluent, such as coagulation–flocculation, ion exchange, membrane filtration, advanced oxidation processes (AOPs), and biodegradation.[8] The high operational cost, tendency to generate sludge, dependency on chemicals, and high energy intake often limit the implementation of these processes.[10,11] Adsorption can overcome these limitations due to its efficiency, flexibility, and cost-effectiveness. Bio-based, green, and low-cost adsorbents derived from agricultural and lignocellulosic biomass have attracted researchers to eliminate dye contaminants. Water hyacinth (*Eichhornia crassipes*) has emerged as a promising candidate in this field. Some recent reviews have highlighted the remarkable potential of *Eichhornia crassipes* to act as an efficient biosorbent for a wide variety of pollutants.[12] In Bangladesh, water hyacinth spreads rapidly across rivers and canals and clogs waterways, making navigation difficult and crowding out native aquatic plants.[13] Moreover, the dense mats of water hyacinth plants often block sunlight penetration, leading to reduced photosynthesis in aquatic plants and depletion of dissolved oxygen, which can subsequently cause death to aquatic plants, organisms and fish.[14] Transforming this invasive waste material into value-added products such as adsorbents presents an opportunity to contribute to circular economy principles as well as waste-to-resource approaches.

Biochar, a carbon-rich porous solid produced through pyrolysis of biomass under limited oxygen conditions, has gained growing interest for pollutant remediation. Recently, it has manifested as an efficient adsorbent for various contaminants, including dyes, pesticides, heavy metals, antibiotics, phenolic compounds, pathogens, microplastics, *etc.* Various bioadsorbents have been explored in the literature as precursors for biochar production, particularly to adsorb dye moieties, such as rice husk,[15] coconut shell,[16] sugarcane bagasse,[17] seaweed,[18] palm residues,[19] invasive plant species,[20] banana peel,[21] groundnut shell,[22] mahagoni wood and bark,[23] *etc.*

Feedstocks are pyrolyzed at various temperatures to produce biochar with diverse structural and chemical features.[24] Studies have demonstrated the applicability of biochar to remove cationic and anionic dyes under different operational conditions. The pyrolysis conditions play a vital role in altering the physicochemical properties, which subsequently affects the adsorption performance. Biochar typically exhibits a higher surface area, abundant porosity, more functional groups, and improved aromaticity as compared to raw biomass. These properties majorly depend on the feedstock type and calcination temperature. The enhanced features after pyrolysis can influence the interaction between dye molecules and the biochar surface mechanism.[25,26] Activation of the biochar physically or chemically has also been reported to enhance the adsorption efficiency.[27] These include multiple preparation stages, instrumental facilities, and the involvement of other chemicals. A facile single-stage pyrolysis route may be beneficial and cost-effective from this perspective. Pristine biochar derived from water hyacinth has received limited attention for its role in removing anionic reactive dyes from textile effluents.

In light of these gaps, the present study focuses on the preparation of a non-toxic pristine biochar from water hyacinth through a facile single-stage slow pyrolysis method for the abatement of reactive dyes from aqueous solution. It involves calcination under a N_2 flow at different temperatures (300, 500, and 700 °C). Reactive Yellow 176 (RY176) was chosen as the model pollutant to reflect the real-world conditions of wet processing industries in Bangladesh. The objective of this study was to investigate the impact of pyrolysis temperatures on the physical, chemical, and interfacial properties of biochars and consequent reactive dye adsorption in solution. The adsorption mechanism of dye molecules and its spontaneity were evaluated with adsorption isotherms, kinetics, and thermodynamic parameters. This study critically analyzed water hyacinth-derived biochars as sustainable and effective adsorbents for anionic dye remediation.

2 Materials and methods

2.1. Reagents and materials

For this study, water hyacinth (*Eichhornia crassipes*) plants were collected from a random local pond near Ashulia, Gazipur, Bangladesh. C.I. Reactive Yellow 176 (RY176) dye was obtained from Dystar, Bangladesh. All other reagents used in the experiments were of laboratory grade and applied without further purification.

2.2. Preparation of water hyacinth (WH) biochar

After collection, roots and flowers of *Eichhornia crassipes* were removed, and the remaining stems and leaves were thoroughly washed with tap water to remove surface impurities. The

biomass was sun-dried for over a month, followed by oven drying at 103 °C for 12 h to eliminate residual moisture, according to ASTM D2867-10.[28] The dried material was chopped (<10 mm), ground (Philips, 750 W, India), and sieved to obtain particles of 100–420 μm, then stored in polyethylene bags before pyrolysis.

Biochars were produced in a laboratory-scale fixed-bed batch reactor placed inside a programmable muffle furnace. Dried biomass was placed inside the reactor vessel, which was consisted of a sealed stainless-steel chamber with a nitrogen gas inlet and exhaust gas outlet. To establish oxygen-limited conditions, high-purity nitrogen gas was purged at a flowrate of 10 L h^{-1} 30 min before heating to displace residual air and maintained continuously throughout the heating until cooling. Pyrolysis was conducted at target temperatures of 300 °C, 500 °C, and 700 °C separately, maintaining a constant heating rate of 5 °C min^{-1} and a residence time of 1 h at the final temperature. The synthesized biochars were denoted as 300BC, 500BC, and 700BC. Each biochar sample was allowed to cool under ambient conditions naturally and continuous nitrogen flow and then preserved in sealed containers to avoid moisture and oxygen contact. Yield was estimated from the weight difference between the initial biomass and resultant biochar. A biochar to water ratio of 1 : 30 (w v^{-1}) was maintained while evaluating pH. A schematic representation of the pyrolysis procedure is shown in SI Fig. S1.

2.3. Characterization

Elemental composition (C, H, and N) was determined using an elemental analyzer (EA3000, Eurovector, Italy), while O content was estimated by difference. Atomic ratios (H/C, O/C, and C/N) were calculated from elemental data. Proximate analysis (moisture, volatile matter, and ash) was carried out according to ASTM methods; fixed carbon was obtained by difference. Biochar yield was expressed as the weight ratio of biochar to the feedstock. Table 1 represents the general characteristics of *Eichhornia crassipes* before and after pyrolysis. The pH of biomass and biochars was measured in 1 : 10 (w v^{-1}) suspensions, and pH_{pzc} was determined by the drift method. Surface functional groups were characterized by FTIR (4000–400 cm^{-1}, Shimadzu FTIR-8400, Japan). Surface morphology was analyzed using a Field Emission Scanning Electron Microscope (FE-SEM) at a 5.0 kV operating voltage, equipped with an energy dispersive spectrometer (JEOL JSM-7600F, Japan) to simultaneously measure the surface elemental composition of the biochars. Thermal stability was assessed by TGA-DTG analysis (40–700 °C, 10 °C min^{-1}, and argon flow 70 mL min^{-1}) using a simultaneous thermal analyzer (NETZSCH STA 449 Jupiter, Germany). Mineral phases were identified by XRD (Empyrean, PANalytical, Netherlands) using Cu-Kα radiation (wavelength: Kα1 = 1.540 598 Å and Kα2 = 1.544 426 Å; 2θ = 10 to 80°). Nitrogen adsorption–desorption isotherms were recorded at 77 K (BELSORP MAX II, Microtrac MRB). The samples were degassed at 150 °C for 2 h prior to analysis. The BET specific surface area (BET_{SSA}) was determined in the P/P_0 range of 0–0.99, while pore volume and size distribution were calculated using the NLDFT-GCMC model.

2.4. Adsorption experiments

2.4.1. Batch adsorption tests. Batch adsorption was carried out by adding a known amount of biochar to 20 mL of dye solution and agitating on a thermostatic shaker at 150 rpm until equilibrium. The dye concentration was quantified using a calibration curve (λ_{max} = 417 nm) by UV-Vis spectrophotometry (UV-1800, Shimadzu, Japan). The adsorption capacity (q_e, mg g^{-1}) and dye removal efficiency (R%) of the biochar were calculated from eqn (1) and (2),[29] respectively:

$$q_e = \frac{(C_0 - C_e)V}{m} \quad (1)$$

$$R(\%) = \frac{(C_0 - C_e) \times 100}{C_0} \quad (2)$$

Table 1 Physicochemical attributes of raw biomass and biochars at different pyrolysis temperatures[a]

Sample	Raw biomass	300BC	500BC	700BC
Yield%	—	46.6 ± 0.35[a]	28.6 ± 0.45[b]	25.3 ± 0.20[c]
pH	7.10 ± 1.20[a]	7.80 ± 0.17[a]	8.30 ± 0.17[b]	10.40 ± 0.26[c]
C%	37.77 ± 0.55[a]	50.84 ± 0.62[b]	56.84 ± 0.47[c]	59.20 ± 0.50[c]
N%	1.98 ± 0.35[a]	2.46 ± 0.35[a]	2.01 ± 0.31[a]	2.03 ± 0.21[a]
H%	6.61 ± 0.40[a]	5.39 ± 0.40[b]	2.18 ± 0.25[c]	1.60 ± 0.30[c]
O%	44.70 ± 1.31[a]	29.95 ± 0.85[b]	16.35 ± 0.65[c]	11.58 ± 1.06[c]
H/C	2.08 ± 0.13[a]	1.26 ± 0.10[b]	0.46 ± 0.05[c]	0.32 ± 0.06[c]
O/C	0.89 ± 0.03[a]	0.44 ± 0.01[b]	0.22 ± 0.01[c]	0.15 ± 0.01[c]
C/N	22.28 ± 3.90[a]	24.07 ± 3.40[a]	32.97 ± 5.08[b]	34.10 ± 3.54[b]
(O + N)/C	1.24 ± 0.04[a]	0.64 ± 0.02[b]	0.32 ± 0.01[c]	0.23 ± 0.02[c]
Moisture%	8.54 ± 1.06[a]	6.94 ± 0.85[a]	2.96 ± 0.45[b]	1.04 ± 0.51[c]
VOC%	79.56 ± 1.08[a]	57.91 ± 1.06[b]	33.55 ± 0.57[c]	33.27 ± 0.45[c]
Ash content%	8.92 ± 1.06[a]	11.36 ± 0.25[b]	22.62 ± 0.20[c]	25.60 ± 0.86[c]
Fixed carbon%	2.98 ± 1.85[a]	23.80 ± 1.38[b]	40.87 ± 0.75[c]	40.09 ± 1.10[c]

[a] Values are expressed as mean ± standard deviation (n = 3). Superscript letters (a, b, and c) within a row indicate statistically significant differences among biochar samples at $p < 0.05$, determined by one-way ANOVA.

where C_0 and C_e (mg L^{-1}) are the initial and equilibrium dye concentrations, respectively, V (L) is the solution volume, and m (g) is the mass of biochar.

The effect of pH was studied in the range of 2–10. Adsorption isotherms were recorded at initial dye concentrations of 10–200 mg L^{-1}.

2.4.2. Adsorption isotherms. Equilibrium isotherm data were analyzed by nonlinear fitting using Langmuir, Freundlich, and Dubinin–Radushkevich (D–R) models.[30] According to the Langmuir model, once a dye molecule adheres to an active site on the adsorbent surface, no further adsorption can occur at that particular site. The process is governed by a state of dynamic equilibrium, where the rates of adsorption and desorption become equal. All available active sites are fully occupied at that stage, indicating that the surface has reached saturation.[31] The model assumes homogeneous monolayer adsorption and is expressed as eqn (3)

$$q_e = \frac{q_{max} K_L}{1 + K_L C_e} \quad (3)$$

where q_{max} (mg g^{-1}) and K_L (L mg^{-1}) account for the maximum adsorption capacity and Langmuir constant, respectively. Its separation factor, R_L, was used to evaluate adsorption favorability as follows (eqn (4)):

$$R_L = \frac{1}{1 + K_L C_e} \quad (4)$$

where R_L indicates the nature of adsorption; the lower the value of R_L, the greater is the favorability; ($R_L > 1$: unfavorable; $R_L = 1$: linear, $0 < R_L < 1$: favorable, $R_L = 0$: irreversible).[31]

The Freundlich isotherm model, originally proposed by Freundlich in 1960, describes adsorption occurring on heterogeneous surfaces. It reflects a chemical adsorption process in which interactions among adsorbed molecules are influenced by heat and energy dissipation. It is particularly suitable for systems with high adsorption capacity at low solute concentrations. The Freundlich model accounts for heterogeneous multilayer adsorption (eqn (5)) and is expressed as follows:

$$q_e = K_F C_e^{\frac{1}{n}} \quad (5)$$

where K_F ($mg^{1-1/n}$ $L^{1/n}$ g^{-1}) and n represent the Freundlich adsorption constant and intensity, respectively.

The three parameter Dubinin–Radushkevich (D–R) isotherm model was applied to explain adsorption on heterogeneous surfaces[32] and establish the relation between the amount of adsorbate retained and the Polanyi potential. The mean free energy was calculated using eqn (6).

$$q_e = q_{max} \exp^{(-\beta\varepsilon^2)} \quad (6)$$

The Polanyi potential (ε, kJ $mmol^{-1}$) was calculated using the following equation (eqn (7)):

$$\varepsilon = RT \ln\left(1 + \frac{1}{C_e}\right) \quad (7)$$

where R is the ideal gas constant (8.31 J mol^{-1} K^{-1}), and T is the temperature on the Kelvin scale.

The mean free energy of adsorption, E (kJ $mmol^{-1}$) was calculated using eqn (8).

$$E = \frac{1}{\sqrt{2\beta}} \quad (8)$$

where β represents the mean free adsorption coefficient ($mmol^2$ kJ^{-2}), which provides insight into the adsorption phenomenon (physical, chemical, or ion-exchange).[33]

2.4.3. Adsorption kinetics. Experiments were conducted over 0–300 min with fixed intervals for the assessment of adsorption kinetics. Pseudo-first order (PFO), pseudo-second order (PSO), and intraparticle diffusion (IPD) models were implemented for analyzing the kinetics and mechanisms.[34,35]

The PFO model assumes a molecular mechanism without dissociation of the adsorbate and is represented as eqn (9):

$$q_e = q_e(1 - e^{-k_1 t}) \quad (9)$$

The PSO model is based on the assumption of chemisorption governing the adsorption process through sharing and exchange of electrons and is mathematically expressed as eqn (10):

$$q_t = \frac{q_e^2 k_2 t}{1 + q_e K_2 t} \quad (10)$$

The intraparticle diffusion (IPD) model accounts for the possibility of multiple rate-limiting steps during adsorption, including boundary layer diffusion and pore diffusion. This model is particularly useful to identify whether the internal pore structure governs the overall kinetics. The linear form was applied to the experimental data and is presented in eqn (11):

$$q_t = K_{id} t^{\frac{1}{2}} + C \quad (11)$$

where K_{id} (mg g^{-1} $min^{-1/2}$) is the intra-particle diffusion rate constant indicating the extent of dye migration within the pores of the adsorbent, and C (mg g^{-1}) reflects the influence of the boundary layer. C gives an idea about the thickness of the boundary layer (*i.e.*, the larger the values of C, the greater is the boundary layer effect). q_t (mg g^{-1}) denotes the adsorption capacity at time t, and q_e (mg g^{-1}) represents the equilibrium adsorption capacity. The constant K_1 (min^{-1}) corresponds to the rate constant of the PFO model, while K_2 (g mg^{-1} min^{-1}) is the rate constant of the PSO model. The intraparticle diffusion rate constant is denoted by K_{id} (mg g^{-1} $min^{1/2}$).

2.4.4. Thermodynamic study. Adsorption thermodynamics were investigated at 10–50 °C. Gibbs free energy change (ΔG), enthalpy change (ΔH), and entropy change (ΔS) were determined from equilibrium constants[36] using eqn (12) and (13):

$$\triangle G = -RT \ln(K_L^0) \quad (12)$$

$$\ln(K_L^0) = \frac{\Delta S}{R} - \frac{\Delta H}{RT} \quad (13)$$

where R (8.314 J mol^{-1} K^{-1}) is the gas constant, T (K) is the absolute temperature, and K_L^0 is the equilibrium distribution coefficient, derived from isotherm constants. For the Langmuir

and the Freundlich models, K_L^0 is expressed as eqn (14) and (15), respectively:

$$K_L^0 = \frac{K_L\ [\text{adsorbate}]^0}{\gamma} \quad (14)$$

$$K_L^0 = \frac{K_F \rho}{1000}\left(\frac{10^6}{\rho}\right)^{\left(1-\frac{1}{n}\right)} \quad (15)$$

where $[\text{adsorbate}]^0$ (1 mol L^{-1}) is the standard concentration of the adsorbate, γ is the activity coefficient, and ρ is the density of water. This approach has been adopted in several previous reports to calculate consistent parameters of thermodynamics.[30,37] The Van't Hoff plot of $\ln(K_L^0)$ *versus* $1/T$ was employed to estimate ΔH and ΔS from the slope and intercept, respectively.

2.4.5. Data analysis. All experiments were performed in triplicate to ensure reproducibility. OriginPro 2024 software was used to analyze the isotherm, kinetics, and thermodynamic data. The goodness-of-fit for each model was assessed by using the correlation coefficient (R^2), chi-square (χ^2), and root mean square error (RMSE). A higher R^2 value coupled with lower χ^2 and RMSE values indicated that a strong agreement exists between experimental and predicted data.

3 Results and discussion

3.1. Biochar characterization

3.1.1. Ultimate & proximate analysis. The proximate analysis demonstrated that the yield significantly reduced in 500BC (28.6%) and 700BC (25.5%) from 46.6% in 300BC, attributed to the major devolatilization of cellulose and lignin decomposition at high temperatures (>300 °C)[38,39] (Table 1). Subsequently, the fixed carbon amount depicted a ~72% increase in 500BC from 300BC, and then attained this stable value even in 700BC. This phenomenon indicates that the primary devolatilization process concluded around 500 °C, and the major aromatization and char stabilization process were guided by the slow degradation of residual H and O compounds at elevated temperatures.[40] Higher pyrolysis temperatures resulted in substantially higher ash content (300BC: 11.4%, 500BC: 22.6% and 700BC: 25.6%) in biochars, ascribed to the primary devolatilization of organic components and progressive concentrations of inorganic minerals such as K, Ca, Mg, Si, *etc.* The proximate analysis of oven dried raw biomass indicated ~8.5% residual moisture. Literature reports suggest that sun dried water hyacinth typically retains ~10–15% moisture depending on ambient conditions,[41] which aligns with the expected reduction before oven drying. The moisture % progressively decreased with temperature in prepared biochars indicating advanced carbonization and increased hydrophobicity at high pyrolysis temperature.

Ultimate analysis revealed that the carbon content in biochar samples demonstrated an incremental relationship with increasing pyrolysis temperature. The increase from 50.84% carbon content in 300BC to 56.84% in 500BC and 59.2% in 700BC was driven by dehydration, decarboxylation, decarbonylation, and cracking reactions, directly correlating with the higher energy density (high HHV), stable aromatization, increased stability, and pore evolution of 500BC and 700BC.[42] The concomitant shift in the polarity index (calculated as (O + N)/C) from 0.64 to 0.23, due to subsequent decline of H (5.39% to 1.6%) and O (30% to 11.6%) content in biochars, reflects this elemental redistribution, as documented by Li *et al.* (2022)[39] (decrease from 0.788 to 0.696 in water hyacinth-derived biochar) and Zhang *et al.* (2022)[42] (decrease from 0.788 to 0.696 in sludge-derived biochar) in previous studies. Additionally, decreasing H/C and O/C atomic ratios indicated enhanced aromaticity and carbon condensation at elevated temperatures. Such structural evolution is generally favorable for dye adsorption, particularly through π–π electron donor–acceptor interactions with aromatic dye molecules.[43]

3.1.2. Fourier transform infrared (FTIR) analysis. FTIR spectroscopy was employed to identify the chemical functional groups present on the surface of biochars. The FTIR spectra of all biochars, along with the raw biomass, are presented in Fig. 1a. The FTIR results revealed notable changes including the emergence of some new groups at higher pyrolysis temperature. In addition, some functional groups originally present in the feedstock gradually disappeared, particularly in 500BC and 700BC. These groups are known to influence the sorption behavior toward anionic dyes.

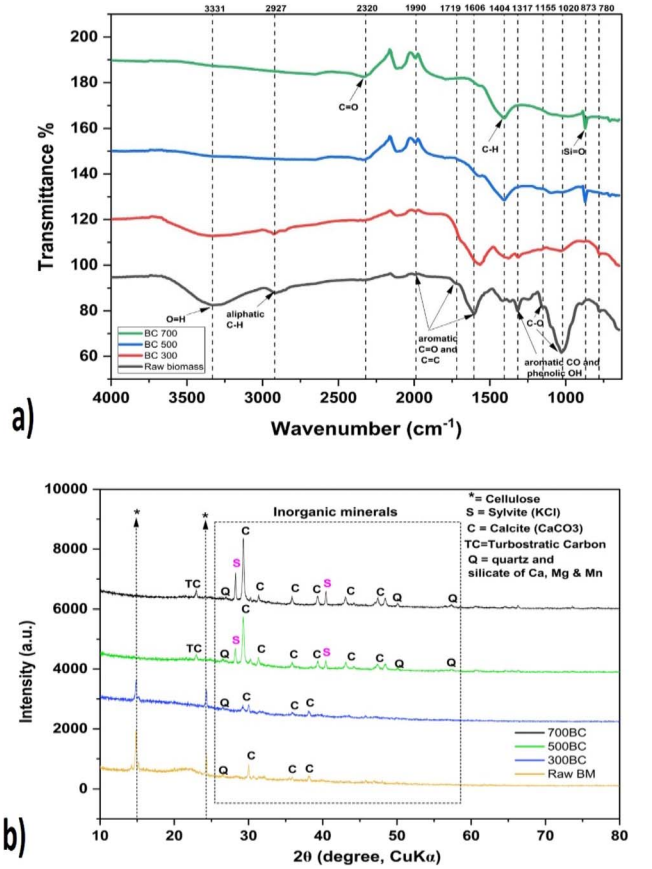

Fig. 1 (a) FTIR (b) X-ray diffractogram of raw biomass (Raw BM) and biochars pyrolyzed at 300 °C (300BC), 500 °C (500BC) and 700 °C (700BC).

The band at 3331 cm^{-1} represented stretching vibrations of the –OH group, which could be attributed to the adsorbed water on the biochar, which was progressively diminished with the increasing pyrolysis temperature.[38] An indication of decreased non-polar aliphatic fraction in 500BC and 700BC was observed, as the band at 2926 cm^{-1} (asymmetric C–H stretching) was primarily associated with aliphatic functional groups in RawBM and 300BC.[39] Furthermore, pyrolysis temperature contributed to increasing the aromatic C═O and C═C groups indicated by the bands at 1990 cm^{-1} and reducing the same around 1719 cm^{-1} and 1606 cm^{-1}.[44–46] Meanwhile, the phenolic –OH or aromatic CO- stretching vibrations in RawBM and 300BC were indicated by the band around 1317 cm^{-1}. The polar groups remarkably decreased when heated beyond 300 °C.[39] Strong peaks at 1020 cm^{-1} for C–O and C═O bond stretching gradually diminished in 500BC and 700BC, confirming complete thermal decomposition of oxygenated groups, cellulose, and hemicellulose, which resulted in volatile evolution and reduction in oxygen content (30% to 11.6% *via* ultimate analysis).[47,48]

3.1.3. Surface morphology analysis by Scanning Electron Microscopy (SEM). The scanning electron microscopy analysis revealed a compact and relatively smooth raw BM surface with minor observable porosity (Fig. 2a). This feature is characteristic of lignocellulosic biomass, as the structural integrity of cellulose, hemicellulose, and lignin limits the development of accessible pores. Mujtaba *et al.* (2023)[49] previously observed similar trends in plant-based materials in their studies. Although the overall morphology of 300BC biochar remained dense with limited pore formation, slight surface roughness and structural degradation were initiated as observed in Fig. 2b, attributed to the low pyrolysis temperature, incomplete volatilization, and minimal disruption in the carbon matrix.[50] SEM images of 500BC (Fig. 2c) revealed a porous structure layered with textures and cracks on the surface. The enhancement in surface heterogeneity and matrix disruption resulted from the thermal decomposition of cellulose and lignin molecules at 500 °C.[51] SEM analysis of 700BC (Fig. 2d) demonstrated a highly porous carbon matrix, ascribed to the synergistic impacts of devolatilization and structural condensation.[52] The increased heterogeneity and interconnected pores facilitate the dye adsorption onto the surface of 700BC through pore filling, electrostatic interactions, and π–π interactions.

3.1.4. Elemental composition analysis by energy dispersive X-ray spectroscopy (EDS). Energy Dispersive X-ray Spectroscopy (EDS) analysis (SI file Fig. S2 and Table 2) revealed that carbon content gradually increased in the biochar ((30–35% by weight)) with increasing pyrolysis temperature, along with a simultaneous reduction in oxygen content to ∼43% in 500BC and ∼45% in 700BC, and nitrogen content to ∼21% in 500BC and ∼45% in 700BC. The marked reductions in O and N content are governed by the concurrent impacts of thermal degradation of organic components (cellulose, hemicellulose, and lignin) and condensation of polycyclic aromatic compounds.[53,54] The reduction in the polarity index confirms extensive degradation of hydrophilic groups (O–H and C–O) through dehydration and decarboxylation (complemented by FTIR). The increment in inorganic elements such as K, Ca, Si, and Mn in biochars with increasing pyrolysis temperature signifies the concentration effect of the inorganic phase with gradual decomposition of the organic matrix. The inorganic components supply multivalent cations (Ca^{2+}, Mn^{2+}, *etc.*) to the biochar surface and elevate the pH of the solution, directly promoting anionic dye adsorption through electrostatic interactions and ion exchange mechanisms.[55,56]

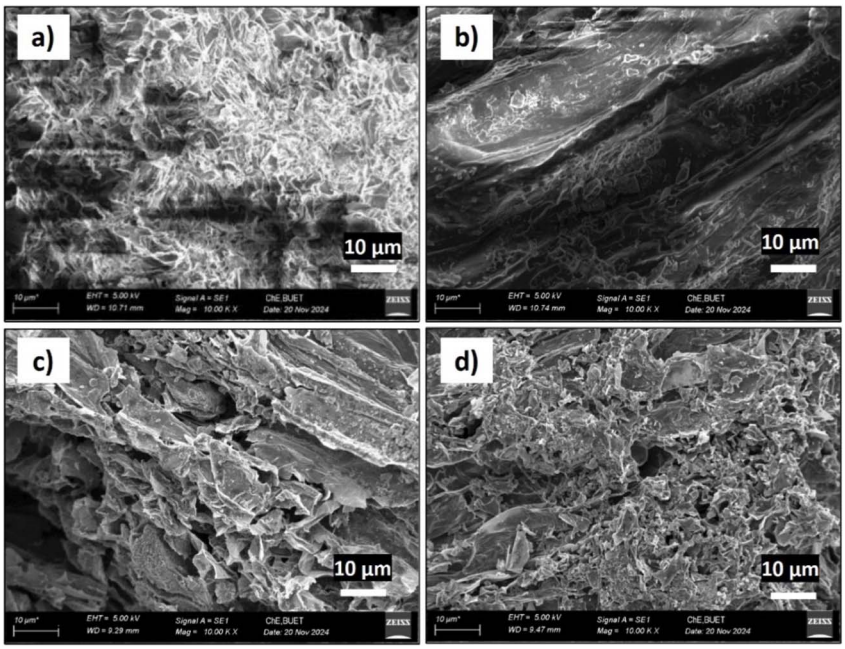

Fig. 2 Scanning electron micrographs (SEM) of (a) raw biomass, (b) 300BC, (c) 500BC, and (d) 700BC, captured at 100 00× magnification. Imaging conditions: an accelerating voltage of 5.00 kV.

Table 2 Elemental composition (weight % and atomic %) by EDS of raw biomass and biochar samples produced at 300 °C, 500 °C, and 700 °C by SEM-EDS analysis[a]

	Raw biomass		300BC		500BC		700BC	
Element	Weight %	Atomic %	Weight %	Atomic %	Weight %	Atomic %	Weight %	Atomic %
C	31.45 ± 1.50[a]	39.43 ± 1.80[a]	41.08 ± 1.60[b]	49.68 ± 1.90[b]	55.48 ± 1.80[c]	66.79 ± 2.10[c]	53.12 ± 1.75[c]	66.09 ± 2.10[c]
N	3.31 ± 0.30[b]	3.56 ± 0.35[b]	4.12 ± 0.35[a]	4.28 ± 0.38[a]	3.26 ± 0.30[b]	3.37 ± 0.35[b]	2.28 ± 0.25[c]	2.43 ± 0.28[c]
O	57.35 ± 2.00[a]	53.97 ± 2.20[a]	47.77 ± 2.10[b]	43.36 ± 2.00[b]	27.25 ± 1.50[c]	24.62 ± 1.40[c]	26.32 ± 1.40[c]	24.58 ± 1.30[c]
Si	0.68 ± 0.10[a]	0.36 ± 0.08[a]	1.08 ± 0.12[b]	0.56 ± 0.10[b]	1.33 ± 0.14[b]	0.68 ± 0.10[b]	1.05 ± 0.12[b]	0.56 ± 0.10[b]
P	0.79 ± 0.12[b]	0.38 ± 0.10[b]	0.62 ± 0.10[a]	0.29 ± 0.08[a]	0.68 ± 0.10[a]	0.32 ± 0.08[a]	0.72 ± 0.10[a]	0.35 ± 0.08[a]
K	2.66 ± 0.25[a]	1.03 ± 0.20[a]	2.75 ± 0.28[a]	1.02 ± 0.22[a]	4.28 ± 0.35[b]	1.58 ± 0.25[b]	6.15 ± 0.40[c]	2.35 ± 0.30[c]
Ca	2.29 ± 0.20[b]	0.86 ± 0.18[b]	1.32 ± 0.18[a]	0.48 ± 0.15[a]	6.14 ± 0.40[c]	2.21 ± 0.30[c]	8.10 ± 0.45[d]	3.02 ± 0.35[d]
Mn	1.46 ± 0.15[b]	0.40 ± 0.10[b]	1.25 ± 0.16[a]	0.33 ± 0.10[a]	1.58 ± 0.18[b]	0.42 ± 0.12[b]	2.26 ± 0.20[c]	0.62 ± 0.12[c]

[a] Values are expressed as mean ± standard deviation ($n = 3$). Superscript letters (a, b, c, and d) within a row indicate statistically significant differences among biochar samples at $p < 0.05$, determined by one-way ANOVA.

3.1.5. X-ray diffraction (XRD) analysis. X-Ray diffraction results demonstrated characteristic Bragg peaks at 14.7° and 22.8° in raw water hyacinth biomass (Fig. 1b) associated with two distinct lattice planes (1–10 and 200) of crystalline cellulose Iβ.[57] The gradual dissipation of these peaks with increasing pyrolysis temperature signifies extensive volatilization of crystalline cellulose domains. The thermal degradation of organic components and aromatization accelerated the shift towards a more ordered graphitic and hydrophobic structure of the carbon matrix.[24,58] This transformation is directly supported by the progressive reduction and eventual disappearance of C–O stretching vibrations at ~1020–1155 cm^{-1} as shown in the FTIR spectra (Fig. 1a). The emergence of sharp peaks at 29.9°, 31.4°, 35.1°, and 38.1° for high pyrolysis temperatures (500BC and 700BC) indicates the formation of crystalline inorganic minerals such as KCl, SiO_2, and $CaCO_3$ (confirmed by the presence of K, Ca, and Si in EDX spectra) within the BC matrix. Concurrently, a low intensity peak at 24.4° for 500BC and 700BC corresponding to the (002) diffraction plane of turbostratic carbon suggests enhanced aromaticity, active adsorption sites, and intercalation capacity, which aids the adsorption mechanisms of dye molecules.[59]

3.1.6. Thermogravimetric analysis (TGA) and derivative thermogravimetry (DTG) analysis. The TGA-DTG analysis demonstrated three distinct thermal degradation stages (Fig. 3), consistent with the lignocellulosic decomposition pathway.[60] The first stage corresponded to the release of physically bound moisture, low molecular weight hydrocarbons, and light volatiles at approximately 100 °C. Moderate DTG peaks between 150 °C and 200 °C observed in raw biomass (Fig. 3a) and 300BC (Fig. 3b) indicate progressive dehydration and release of low-molecular-weight volatiles associated with early-stage thermal decomposition.[61] Critically, intense peaks in the 250–350 °C range, along with significant mass loss for 300BC, and the results obtained from proximate analysis (Table 1) collectively validate the degradation of inherent hemicellulose and cellulose and incomplete carbonization with some residual moisture and volatile matter. In contrast, higher pyrolysis temperatures (500 °C and 700 °C) resulted in reduced mass and enhanced thermal stability, attributed to the increased devolatilization and formation of aromatic structures, as confirmed by the comparably higher thermal conversion observed in BC500 (Fig. 3c) and BC700 (Fig. 3d).[62] Each biochar sample displayed broad DTG peaks in the range of 350–550 °C, ascribed to the characteristic of the decomposition of carbonaceous residues, partial lignin degradation, and gradual char formation.[63] Increasing pyrolysis temperature resulted in broader DTG signals shifted toward higher temperatures, reflecting the formation of more thermally stable carbon structures with

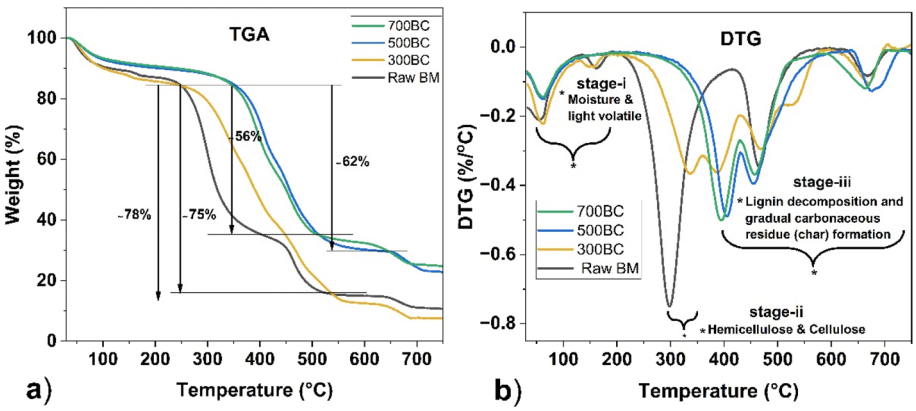

Fig. 3 (a) TGA analysis of raw biomass (raw BM) and biochars pyrolyzed at 300 °C (300BC), 500 °C (500BC) and 700 °C (700BC). (b) DTG analysis of raw biomass (raw BM) and biochars pyrolyzed at 300 °C (300BC), 500 °C (500BC) and 700 °C (700BC).

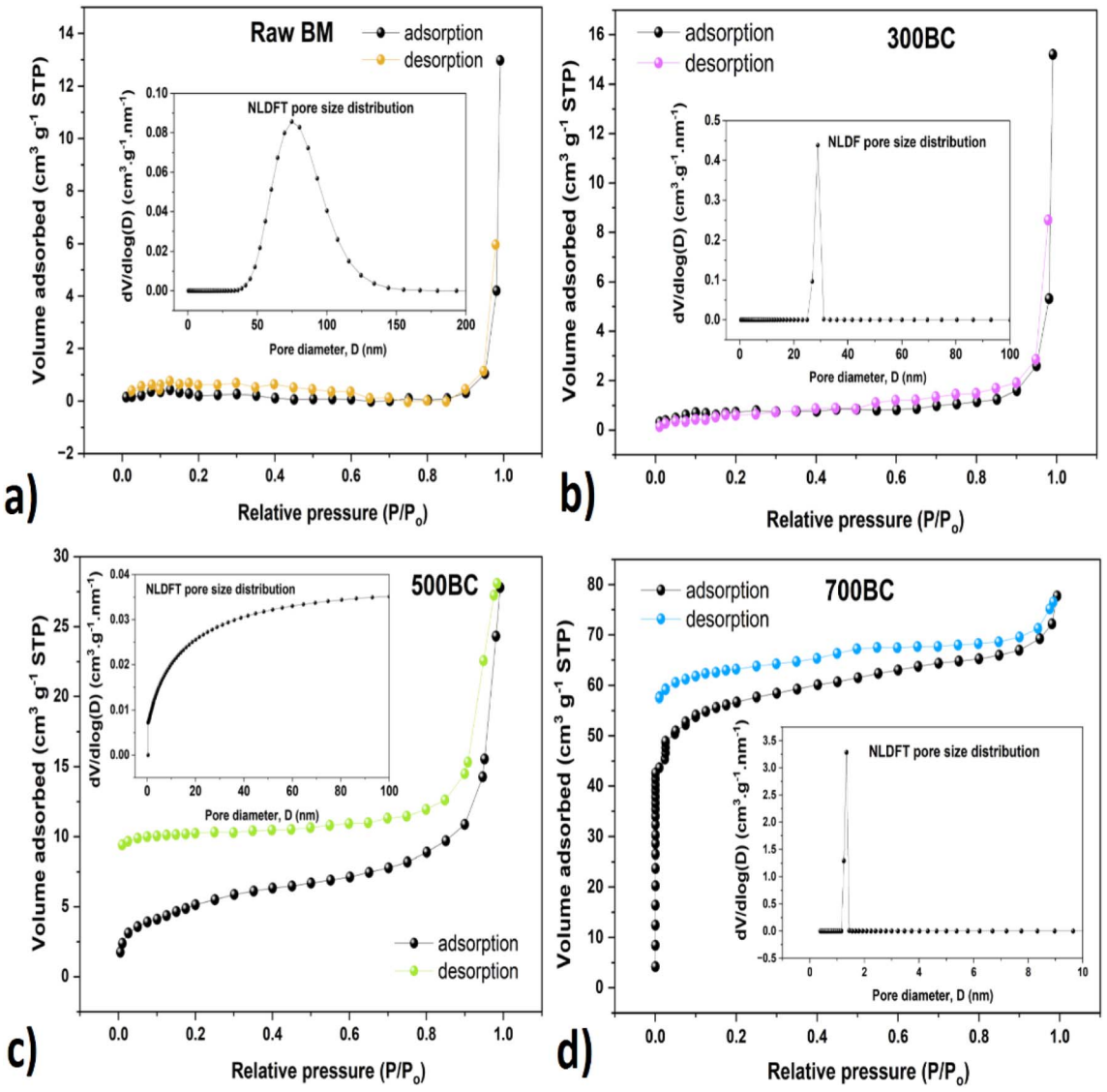

Fig. 4 N_2 adsorption–desorption isotherms of (a) raw biomass (raw BM) and biochars pyrolyzed at (b) 300 °C (300BC), (c) 500 °C (500BC) and (d) 700 °C (700BC) (inset: pore size distribution by the NLDF GCMC model).

higher residual weight percentages of about 23% and 25% for BC500 and BC700, respectively.

3.1.7. Brunauer–Emmett–Teller (BET) surface area and Non-Local Density Functional Theory (NLDFT) for porous structure analysis. N_2 adsorption–desorption isotherms of biomass and biochars are depicted in Fig. 4. Table 3 represents the results of the BET surface area ($m^2\ g^{-1}$), pore volume ($cm^3\ g^{-1}$), and pore size (nm) of raw biomass and biochars, revealing the fact that the physicochemical characteristics of water hyacinth-derived biochars were strongly influenced by pyrolysis temperature. Raw biomass exhibited a very low BET specific surface area (~1.25 $m^2\ g^{-1}$) and a total pore volume of ~0.018 $cm^3\ g^{-1}$. Micropore and mesopore volumes were almost absent, and macropores (calculated by subtraction) dominated, comprising 94% of total pore volume. The isotherm for raw BM was nearly flat at low to mid relative pressure (P/P_0), with a sharp

Table 3 Textural properties of the prepared raw biomass and different biochars

Sample	BET surface area ($m^2\ g^{-1}$)	Total pore volume ($cm^3\ g^{-1}$, $P/P_0 \approx 0.99$)	Micropore volume ($cm^3\ g^{-1}$)	Mesopore volume ($cm^3\ g^{-1}$)	Macropore volume ($cm^3\ g^{-1}$)	Average pore diameter (nm) slit
Raw BM	1.25	0.018	—	0.001	0.017	30.40
300BC	3.59	0.023	—	0.017	0.006	22.13
500BC	30.88	0.067	0.004	0.028	0.035	4.40
700BC	211.31	0.198	0.115	—	—	1.12

uptake near $P/P_0 \approx 0.99$ (Fig. 4a), indicating that pore filling only occurred in large voids and interparticle spaces. This matches a type of isotherm dominated by macropores (>50 nm).[64] In Fig. 4b, the BET surface area slightly increased to ~3.6 $m^2\ g^{-1}$, and the mesopore volume became noticeable (~0.017 $cm^3\ g^{-1}$) for 300BC. A weak hysteresis loop appeared at high P/P_0, indicating underdeveloped mesoporosity. The pore size distribution curve showed mesopores around ~20–30 nm (inset: Fig. 4b). The biochars demonstrated type I and IV isotherms for pyrolysis temperatures over 300 °C.[65] 500BC showed substantial advancement with around a 10-fold increase in the surface area (~30.9 $m^2\ g^{-1}$) and about a 3-fold increase in total pore volume (~0.067 $cm^3\ g^{-1}$) as compared to 300BC. The reduced average pore diameter was 4–5 nm, suggesting mesoporous characteristics (<2 nm). Its isotherm displayed a pronounced hysteresis loop indicating abundant mesoporosity. The pore distribution curve (Fig. 4c) confirmed the emergence of structured mesopores, enhancing adsorption potential.[66] Biochars pyrolyzed at 700 °C demonstrated the most advanced porous structure with about a 7-fold increase of the BET surface area (211.3 $m^2\ g^{-1}$) compared to 500BC (Fig. 4d). The narrow average pore diameter was 1.12 nm. The pore size distribution curve in the inset of Fig. 4d highlighted a major fraction of pore volume in micropores (~0.115 $cm^3\ g^{-1}$), diminishing mesopore and macro contributions. The average pore diameter dropped, consistent with a sharp peak in the micropore range of the pore size distribution curve. The adsorption–desorption isotherm at 700 °C exhibited a steep uptake at low relative pressures, a rapid increase in gas adsorption in the range of $0.9 < P/P_0 < 1.0$, and a wide hysteresis loop, characteristic of micropore (<2 nm) filling and capillary condensation.[67] Such structural evolution of biochar at 700 °C contributed to the highest dye adsorption capacity through the pore-filling mechanism due to the higher specific surface area and pore volume.

These results collectively highlighted the progressive development of micro-, meso-, and macroporosity with increasing pyrolysis temperature, in agreement with previous studies showing that higher temperatures promote pore densification due to loss of volatiles, surface area enhancement, and hysteresis loop expansion due to capillary effects and pore network restructuring.[68,69] Surface areas of all biochars produced in the present study were notably higher than those reported for water hyacinth-derived biochars in previous literature.[38,70] A table is shown comparing the surface area of different biochars derived from lignocellulosic biomass (Table 4).

3.2. Point of zero charge (pH_{pzc}) and influence of pH

Initial solution pH plays a decisive role in adsorption, as it governs both the ionization of dye molecules and the surface charge of adsorbents.[82] The surface pH of the biochars increased from 8 at 300 °C to a strongly alkaline 10.2 at 700 °C (Table 1). This rise can be attributed to the formation of mineral-rich phases, enhanced aromaticity, and a reduction in oxygen-containing functional groups at higher pyrolysis temperatures.[83,84] These trends were further supported by the higher mineral content observed in the elemental analysis (Table 1) and the decreasing H/C and O/C ratios with temperature in the ultimate analysis (Table 1). The point of zero charge (pH_{pzc}) values for 300BC, 500BC, and 700BC were determined to be 8.2, 9.0, and 10.3, respectively (Fig. 5a), indicating that the surfaces were positively charged when the solution pH < pH_{pzc} and became negatively charged at pH > pH_{pzc}. As shown in Fig. 5b, all biochars exhibited the highest adsorption of Reactive Yellow 176 under strongly acidic conditions (pH 3), which can be attributed to the strong protonation of surface functional groups that enhance electrostatic attraction toward the dye's sulfonate ($-SO_3^-$) and sulfatoethylsulfone ($-OSO_3^-$) moieties.[85,86] In contrast, the adsorption capacity decreased gradually as the solution pH increased and electrostatic repulsion between negatively charged biochar surfaces and dye anions became dominant. This may be attributed to the fact that, in a basic medium, dye removal is lower due to the competition between OH^- ions and dye anions for the same active sites on the biochars, a trend supported by the findings of Aichour,

Table 4 BET surface area of biochars derived from lignocellulosic biomasses at different pyrolysis temperatures

[80]Pristine biochar	Pyrolysis temperature (°C)	BET specific surface area ($m^2\ g^{-1}$)	Ref.
Water hyacinth	300, 500, 700	3.5, 19.5, 211	This study
Water hyacinth	300, 500, 700	1.1, 29.8	Gezahegn *et al.*, 2025 (ref. 38)
Water hyacinth	300, 500, 700	2.5, 8.1, 20.9	Liu *et al.*, 2020 (ref. 70)
Water hyacinth	300, 500, 700	3.5, 6.7, 175.4	Li *et al.*, 2016 (ref. 71)
Water hyacinth	600	236.4–347.2	Irewale *et al.*, 2025 (ref. 72)
African almond leaves	700	241	Jabar *et al.*, 2022 (ref. 73)
Pine wood	300, 500	1.2393	Handiso *et al.*, 2024 (ref. 74)
Oil palm	500	0.25–4.4	Palamanit *et al.*, 2019 (ref. 75)
Sawdust	350, 450, 550	2.5,45.7221	Chowdhury *et al.*, 2016 (ref. 76)
Sugar cane bagasse	350	1.3–5.4	Peres *et al.*, 2022 (ref. 61)
Pitch pine	300, 400, 500	2.9,4.8175.4	Kim *et al.*, 2012 (ref. 77)
Wood	700	612	Burachevskaya *et al.*, 2023 (ref. 78)
Rice husk	700	231	Avramiotis *et al.*, 2021 (ref. 79)
Sunflower seed husk	450	3.85	Saleh *et al.*, 2016 (ref. 80)
Wood chips	500	196	Chiu & Huang, 2020 (ref. 81)

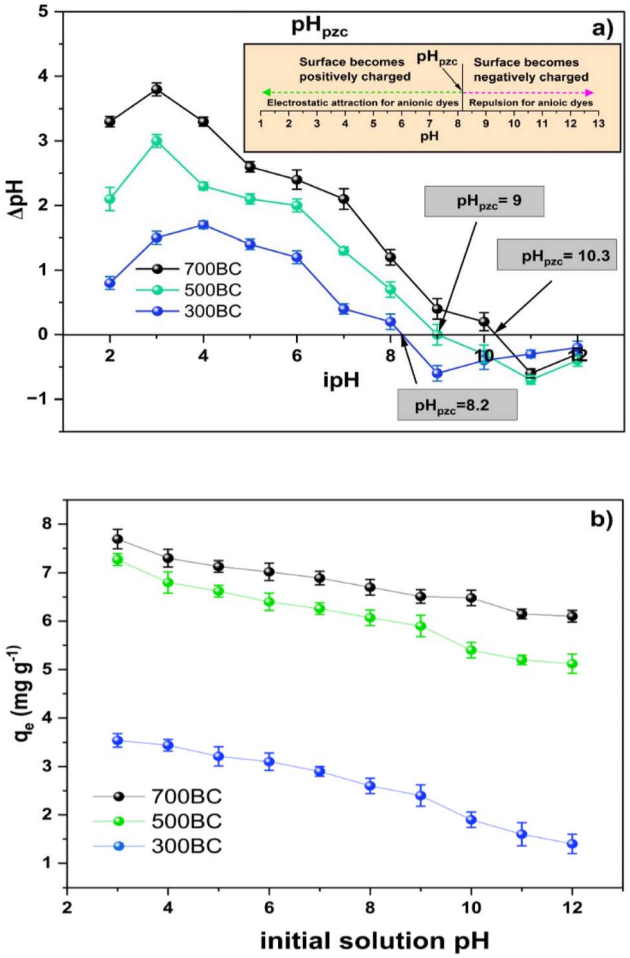

Fig. 5 (a) pH_{pzc} and (b) influence of the solution pH on adsorption capacity of biochars pyrolyzed at 300 °C (300BC), 500 °C (500BC), and 700 °C (700BC).

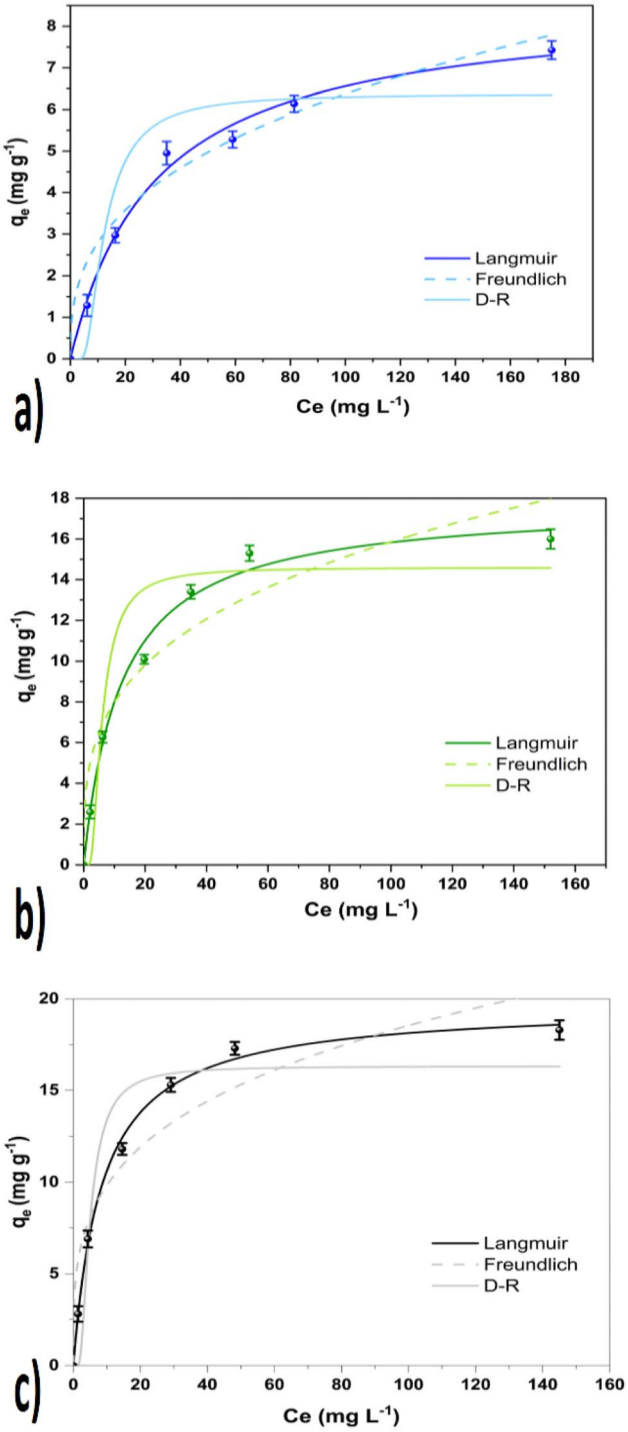

Fig. 6 Non-linear isotherm model fitting for dye adsorption onto all biochars. (a) 300BC, (b) 500BC, and (c) 700BC (biochar loading = 3 g L; pH = 7, temperature = 30 ± 2 °C, contact time = 300 min, stirring rate = 150 rpm).

Zaghouane-Boudiaf, & Khodja (2022).[87] At neutral pH 7, however, the removal efficiencies followed the order: 700BC (83%) > 500BC (75%) > 300BC (35%). This trend reflected the combined effect of higher pH_{pzc} and superior porosity of 700BC, which maintained a net positive charge up to pH ~10.3 and offered abundant accessible sites. Stable adsorption capacity across the pH range of 10–12 for 500BC and 700BC implies that non-electrostatic mechanisms potentially contributed to the dye adsorption process.

From a practical standpoint, the strong pH dependence of adsorption of reactive dyes has important implications for real textile wastewater treatment. Industrial textile effluents are typically discharged at near-neutral to slightly alkaline pH to meet discharge regulations. Although maximum adsorption occurred at pH 3, adjusting large volumes of wastewater under strongly acidic conditions may increase operational costs due to significant acid consumption, corrosion control and additional pH neutralization before discharge. Additionally, this adjustment can potentially complicate the downstream treatment process. Therefore, the comparatively high removal efficiency of 700BC (~83%) at neutral pH 7 highlights its greater suitability for practical applications compared to 300BC (~35%). Future studies may focus on surface modification or composite development to enhance adsorption performance under neutral conditions, thereby improving economic feasibility and scalability.

3.3. Equilibrium isotherm analysis

Nonlinear fitting of the Langmuir, Freundlich, and DR isotherm models is presented in Fig. 6. The adsorption isotherm parameters for all biochars pyrolyzed at different temperatures are summarized in Table 5. The Langmuir model exhibited the best statistical fit at every pyrolysis temperature, revealing monolayer adsorption on homogeneous binding sites on the biochar surface (Table 5). The highest correlation coefficient and lower RMSE and χ^2 values ($R^2 = 0.99$; RMSE = 0.23–0.54; χ^2 = 0.06–0.35) confirmed the goodness-of-fit of the model. The calculated maximum adsorption capacities ($q_{max,cal}$) were also consistent with the corresponding experimental values ($q_{e,exp}$), further validating the suitability of the Langmuir isotherm model to describe reactive dye adsorption onto the studied biochars. This agreement may be attributed to the surface functional groups that provide relatively uniform adsorption energies across the biochar surface during dye uptake.[88] The Langmuir separation factor (R_L) values ranged from 0.14 to 0.77 for 300BC, 0.06 to 0.56 for 500BC, and 0.03 to 0.36 for 700BC, indicating favourable adsorption ($0 < R_L < 1$) across a wide range of initial dye concentrations (10–200 mg L^{-1}). The notable decrement in R_L values with increasing K_L and C_0 values indicates enhanced adsorption favorability for 500BC and 700BC.[89,90]

Alternatively, the Freundlich model demonstrated a reasonably strong fit (R^2 = 0.92–0.96), suggesting that the irregular three-dimensional porous carbon matrix, combined with its large surface area (Fig. 2), facilitated the adsorption mechanism of dye molecules. The favourable Freundlich intensity factor ($1/n$) values (0.28–0.36) confirm high surface heterogeneity of biochar matrices consisting of a variety of binding sites with different energy levels, which effectively promote high pollutant affinity even at low concentrations.

The Dubinin–Radushkevich (D–R) model exhibited increasing R^2 values (0.89, 0.92, and 0.93) with rising pyrolysis temperatures. This indicated a potential contribution of pore-filling mechanisms, particularly for 500BC and 700BC. However, higher RMSE and χ^2 values revealed that its overall fit was comparatively weaker. Although the D–R model approximated q_{max} values across all biochars, it did not provide statistically significant goodness-of-fit. The mean adsorption energy (E), derived from the D–R model, ranged between 0.158 and 0.362 kJ mol^{-1}, indicating that the adsorption of dye molecules onto biochar surfaces occurs predominantly through physisorption.[91] To summarize, the Langmuir isotherm model was identified as the most appropriate and was therefore employed for subsequent analysis.

Table 6 compares the maximum adsorption capacities (mg g^{-1}) of some anionic reactive dyes on pristine water hyacinth-derived biochar with those of other non-modified biochars reported in previous literature. The maximum dye uptake values were presented as calculated from their corresponding isotherm models. In this study, the adsorption performance of water hyacinth-derived biochar was comparable to or even higher than some of the nonactivated biochars derived from diverse biomass sources, *e.g.*, banana peel, coffee fruit shell waste, macadamia nut residue, mahagoni wood and bark, *etc.* Some pristine biochars showed higher adsorption efficiency, which was attributed to differences in dye composition, dye class, and the feedstock type. Several reports also revealed enhanced dye uptake following modification or activation treatments of pristine biochars.[92] Considering pyrolysis without any further modification or activation, the capacity of this biochar confirmed its suitability as a sustainable and competitive adsorbent for the abatement of reactive dyes.

3.4. Kinetics and intraparticle diffusion analysis

The kinetic plots and corresponding parameters are illustrated in Fig. 7a and presented in Table 7, respectively. Initially, the dye adsorption rate was rapid, but it gradually stabilized as

Table 5 Adsorption isotherm parameters of different biochars[a]

Biochar	Langmuir		Freundlich		Dubinin–Radushkevich (D–R)	
300BC	$q_{max,}$ (mg g^{-1})	8.59 ± 0.39	K_F ($mg^{1-1/n}$ g^{-1} $L^{1/n}$)	1.22 ± 0.02	q_{max} (mg g^{-1})	6.37 ± 0.04
	K_L (L mg^{-1})	0.03 ± 0.01	n	2.79 ± 0.03	β	20 ± 0.86
	Reduced χ^2	0.06	Reduced χ^2	0.12	Reduced χ^2	0.88
	R^2	0.99	R^2	0.96	R^2	0.89
	RMSE	0.23	RMSE	0.51	RMSE	0.86
500BC	$q_{max,}$ (mg g^{-1})	17.77 ± 0.64	K_F ($mg^{1-1/n}$ g^{-1} $L^{1/n}$)	4.02 ± 1.02	q_{max} (mg g^{-1})	14.59 ± 0.07
	K_L (L mg^{-1})	0.08 ± 0.01	n	3.35 ± 0.69	β	6.81 ± 0.22
	Reduced χ^2	0.35	Reduced χ^2	3.59	Reduced χ^2	3.88
	R^2	0.99	R^2	0.92	R^2	0.92
	RMSE	0.54	RMSE	1.73	RMSE	1.8
700BC	q_{max} (mg g^{-1})	19.68 ± 0.41	K_F ($mg^{1-1/n}$ g^{-1} $L^{1/n}$)	5.21 ± 1.19	q_{max} (mg g^{-1})	16.33 ± 1.15
	K_L (L mg^{-1})	0.12 ± 0.01	n	3.63 ± 0.75	β	3.58 ± 1.32
	Reduced χ^2	0.18	Reduced χ^2	4.83	Reduced χ^2	4.58
	R^2	0.99	R^2	0.92	R^2	0.93
	RMSE	0.39	RMSE	2.01	RMSE	1.95

[a] Values = mean ± SD. The Langmuir separation factor (R_L) values ranged from 0.14 to 0.77 for 300BC, 0.06 to 0.56 for 500BC, and 0.03 to 0.36 for 700BC, indicating favourable adsorption ($0 < R_L < 1$) across a wide range of initial dye concentrations (10–200 mg L^{-1}). The notable decrement in R_L values with increasing K_L and C_0 values indicates enhanced adsorption favorability for 500BC and 700BC.[89,90]

Table 6 Comparison of the adsorption of some reactive dyes on various pristine biochars

Name of pristine biochar	Pyrolysis temperature (°C)	Reactive dye	Experimental setup	Maximum dye adsorption capacity calculated from the Langmuir isotherm model (mg g^{-1})	Ref.
Water hyacinth	700 °C	Reactive Yellow 176	Initial dye conc.: 10–200 mg L^{-1}, pH: 7, temp. 30 ± 2 °C, contact time: 300 min, and dose: 3.0 g L^{-1}	19.68	This study
Al-based waterworks sludge	800 °C	Reactive Yellow 176	Initial dye conc.: 10–160 mg L^{-1}, pH: 5.5, temp. 20 °C, contact time: 480 min, and dose: 3.3 g L^{-1}	32.154	Wei *et al.* (2023)[93]
Banana peel	500 °C	Reactive black B	Initial dye conc.: 25–150 mg L^{-1}, pH: 3, temp. 27 ± 2 °C, contact time: 120 min, and dose: 8 g L^{-1}	7.58	Kapoor *et al.* (2022)[94]
Coffee fruit shell waste	300 °C	Remazol yellow FG	Initial dye conc.: 10–80 mg L^{-1}, pH: 6, contact time: 200 min, and dose: 8 g L^{-1}	2.42	Sukarta *et al.* (2025)[95]
Seaweed	500 °C	Remazol brilliant blue R	Initial dye conc.: 50–500 mg L^{-1}, pH: 2, temp. 20 °C, contact time: 480 min, dose: 3.3 g L^{-1}	92.5	Vijayaraghavan & Ashokkumar (2019)[18]
Groundnut shell	450 °C	Reactive orange 16	Initial dye conc.: 5–100 mg L^{-1}, pH: 2, temp. 35 °C, contact time: 360 min, and dose: 1 g L^{-1}	80.2	Muralikrishnan & Jodhi (2023)[22]
Coconut shell	400 °C	Remazol black B	Initial dye conc.: 5–100 mg L^{-1}, pH: 2, temp. 35 °C, contact time: 360 min, and dose: 1 g L^{-1}	100.8	Ragunath *et al.* (2023)[16]
Mahagoni wood	200 °C	Reactive red 120	Initial dye conc.: 5–70 mg L^{-1}, pH: 3, temp. 25 ± 2 °C, contact time: 150 min, and dose: 10 g L^{-1}	3.8	Chakraborty *et al.* (2021)[23]
Mahagoni bark	200 °C	Reactive red 120	Initial dye conc.: 5–70 mg L^{-1}, pH: 3, temp. 25 ± 2 °C, contact time: 150 min, and dose: 10 g L^{-1}	5.4	Chakraborty *et al.* (2021)[23]
Rice husk	450 °C	Reactive blue 19	Initial dye conc.: 5–100 mg L^{-1}, pH: 2, temp. 35 °C, contact time: 360 min, and dose: 1 g L^{-1}	98.6	Muralikrishnan & Jodhi (2021)[15]
Manihot esculenta stalk	350 °C	Reactive Yellow dye	Initial dye conc.: 10–50 mg L^{-1}, pH: 7, temp. 27 ± 2 °C, contact time: 45 min, and dose: 1.5 g L^{-1}	53.47	Gajendiran *et al.* (2024)[96]

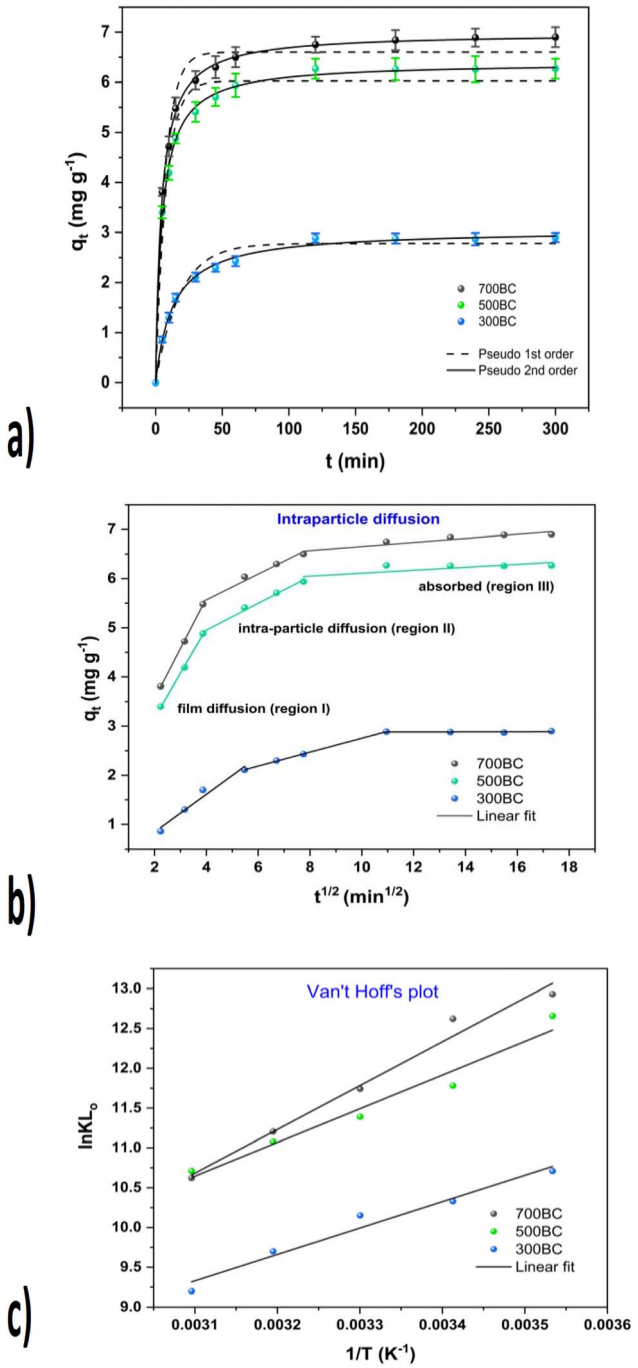

Fig. 7 (a) Non-linear kinetic fitting model, (b) intraparticle diffusion (IPD) model (Linear fit), and (c) Van't Hoff's plot for dye adsorption onto all biochars.

contact time progressed. The amount of dye adsorbed onto all biochar samples increased over the experimental contact time. Kinetic analysis revealed that each biochar sample followed the pseudo-second order model ($R^2 \approx 0.99$, RMSE = 0.6–0.8, and χ^2 = 0.01 and 0.04), indicating that the adsorption mechanism was driven by specific interactions between the biochar surface and adsorbate dye molecules.[97] The initial rapid adsorption is governed by the electrostatic attraction between biochar and dye molecules, followed by subsequent slower stages such as hydrogen bonding with oxygen-containing surface groups and π–π interactions between the aromatic structures of the dye and the graphitic domains of the biochar.[87] The presence of oxygenated functional groups such as –COOH, –C=O, and –OH provided optimum conditions for chemisorption of anionic dye molecules through electrostatic interactions. This rapid electrostatic attraction initiated the mass transfer of dye molecules, promoting stronger hydrogen bonding, π–π interactions, and electron exchange between dye moieties and the biochar surface.[98–100] The intraparticle diffusion (IPD) model, based on the IPD linear model (Table 8), revealed three separate phases in the adsorption phenomenon (Fig. 7b), which confirmed that film diffusion played a pivotal role in the overall adsorption process, followed by intraparticle diffusion in the second phase, and the third phase was referred to as equilibrium pore saturation. In Fig. 7b, the slope of the first phase (R^2 = 0.97–0.99) was consistently higher than that of the second phase (R^2 = 0.97–0.99). This indicated faster film diffusion than internal pore diffusion of dye molecules. This initial phase suggested the presence of abundant active sites on fresh biochars, which gradually became saturated. About 77–79% of the total dye uptake was achieved within the initial 15 min for 500BC and 700BC, and >72% was achieved in 30 min for 300BC. After saturation of surface active sites, pore diffusion became dominant in the second stage until the equilibrium was achieved after 120 minutes. The overall findings suggested that film diffusion was the primary rate-dominating step, whereas pore diffusion acted as the rate-limiting factor for all biochars.[29]

3.5. Thermodynamic analysis

The Van't Hoff plot (Fig. 7c) was used to estimate the change in thermodynamic parameters, enthalpy (ΔH), entropy (ΔS), and Gibbs free energy (ΔG) (summarized in Table 9). The ΔH values (−27.59 to −45.73 kJ mol^{-1}) indicated that the adsorption process was exothermic in nature and primarily governed by surface interactions. Physisorption is associated with ΔH values below 40 kJ mol^{-1} and chemisorption with values above ~80 kJ mol^{-1}; however, intermediate values (40–80 kJ mol^{-1}) may involve combined mechanisms.[101] In this study, the ΔH values of 300BC (−27.59 kJ mol^{-1}) and 500BC (−35.16 kJ mol^{-1}) indicated that the adsorption process was predominantly driven by weak interactions such as van der Waals forces, electrostatic attraction, hydrogen bonding, and π–π interactions, rather than by the formation of strong chemical bonds. Meanwhile, the ΔH value of 700BC (−45.73 kJ mol^{-1}) falls within the transitional range, suggesting that the adsorption process, even though predominantly controlled by weak interactions, can be impacted by strong chemical interactions. This assertion is strongly evident from the superior adsorption capacity demonstrated by 700BC over 300BC and 500BC. Decreased randomness at the solid–liquid interface during adsorption (suggested by consistent negative ΔS values: −7.98 to −52.38 J mol^{-1} K^{-1}) implied that dye molecules transition from a highly disordered state in the bulk solution to a more structured configuration at the biochar–solution interface. The decrease in

Table 7 Kinetic parameters of dye adsorption on biochars[a]

Biochar	Pseudo first-order kinetics		Pseudo second-order kinetics	
300BC	$q_{e,cal}$ (mg g^{-1})	2.78 ± 0.08	$q_{e,cal}$ (mg g^{-1})	3.06 ± 0.04
	K_1 (min^{-1})	0.05 ± 0.01	K_2 (g mg^{-1} min^{-1})	0.03 ± 0.00
	$q_{e,exp}$ (mg g^{-1})	2.9		
	Reduced χ^2	0.03	Reduced χ^2	0.04
	R^2	0.97	R^2	0.99
	RMSE	0.16	RMSE	0.06
500BC	$q_{e,cal}$ (mg g^{-1})	6.03 ± 0.13	$q_{e,cal}$ (g mg^{-1} min^{-1})	6.39 ± 0.04
	K_1 (min^{-1})	0.13 ± 0.01	K_2	0.03 ± 0.00
	$q_{e,exp}$ (mg g^{-1})	6.3		
	Reduced χ^2	0.11	Reduced χ^2	0.01
	R^2	0.97	R^2	0.99
	RMSE	0.31	RMSE	0.08
700BC	$q_{e,cal}$ (mg g^{-1})	6.60 ± 0.13	$q_{e,cal}$ (g mg^{-1} min^{-1})	6.98 ± 0.03
	K_1 (min^{-1})	0.14 ± 0.01	K_2 (g mg^{-1} min^{-1})	0.03 ± 0.00
	$q_{e,exp}$ (mg g^{-1})	6.9		
	Reduced χ^2	0.11	Reduced χ^2	0
	R^2	0.98	R^2	0.99
	RMSE	0.31	RMSE	0.06

[a] Values = mean ± SD.

Table 8 IPD parameters (linear fitting)[a]

Biochar	Parameters	Film diffusion	Intraparticle diffusion	Equilibrium
300BC	C	0.07 ± 0.19	1.34 ± 0.02	2.88 ± 0.05
	K_{id}	0.39 ± 0.05	0.14 ± 0.02	6.79 × 10^{-4} ± 0.03
	RMSE	0.05	0.01	0.01
	R^2	0.97	0.99	0.02
500BC	C	1.36 ± 0.10	3.86 ± 0.11	5.81 ± 0.19
	K_{id}	0.91 ± 0.03	0.27 ± 0.02	0.03 ± 0.01
	RMSE	0.01	0.02	0.06
	R^2	0.99	0.99	0.60
700BC	C	1.51 ± 0.07	4.52 ± 0.17	6.24 ± 0.11
	K_{id}	1.02 ± 0.02	0.26 ± 0.028	0.04 ± 0.01
	RMSE	0.01	0.04	0.03
	R^2	0.99	0.97	0.88

[a] Values = mean ± SD.

entropy values can be attributed to the confinement of dye molecules inside the porous biochar matrices, limiting the translational and rotational freedom. Moreover, formation of interfacial complexes through electrostatic interactions, van der Waals forces, and H-bonding, and ordered π–π stacking interactions between aromatic rings of the RY 176 and graphitic complexes of biochar synergistically reduce the values of ΔS.[101] The variations in ΔG from −24.71 kJ mol^{-1} to 30.42 kJ mol^{-1} suggest that the spontaneity of the adsorption process increased with increasing temperature, aligning with the mechanisms of physisorption. Nevertheless, 500BC and 700BC demonstrated superior adsorptive performance resulting from the synergistic impact of the interconnected porous network, and elevated surface interactions.[102,103]

Table 9 Thermodynamic parameters ($\Delta G°$, $\Delta H°$, and $\Delta S°$) of reactive dye adsorption onto all biochars over the temperature range of 10–50 °C

Biochar	T (K)	ΔH (kJ mol^{-1})	ΔS (J mol^{-1} K^{-1})	ΔG (kJ mol^{-1})
300BC	283	−27.59	−7.98	−25.20
	293			−25.16
	303			−25.57
	313			−25.24
	323			−24.71
500BC	283	−35.16	−19.95	−29.78
	293			−28.70
	303			−28.70
	313			−28.83
	323			−28.77
700BC	283	−45.73	−52.38	−30.42

3.6. Proposed mechanism for dye adsorption

Fig. 8 demonstrates the probable dye adsorption mechanism onto the biochars. The adsorption mechanism was governed by their surface interactions and the intraparticle diffusion process. Kinetic analysis (IPD model) suggested that the initial rapid adsorption of dye molecules occurred due to film diffusion, followed by the rate-limiting step of intraparticle

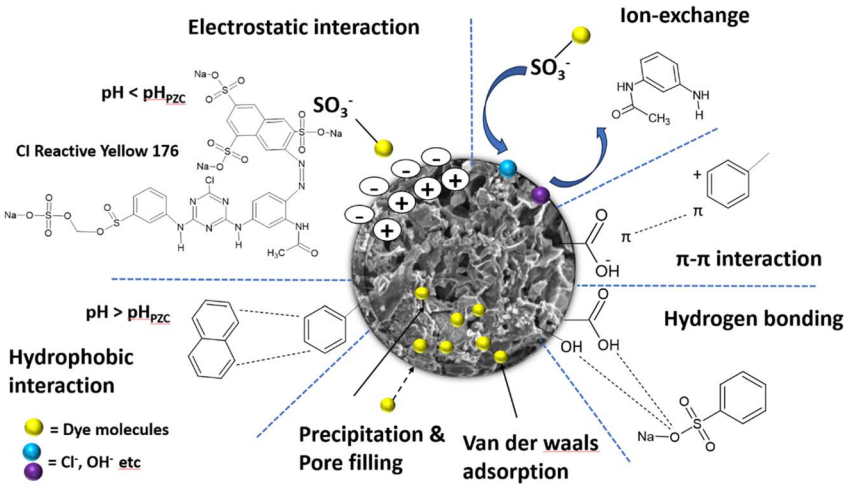

Fig. 8 Adsorption mechanism of Cl Reactive Yellow 176 on water-hyacinth-derived biochars.

diffusion.[97] The strong fit with the Langmuir isotherm model suggested monolayer adsorption on the biochar surface.[104] Additionally, ΔH values < 50 kJ mol^{-1} confirm the physisorptive nature of the adsorption process. Film diffusion facilitated the pore filling mechanism inside the BC matrix, aiding the van der Waals interactions between the internal surface of the biochar and dye molecules. The solution pH (below pH_{pzc} = 8.0–10.5) generated a positive charge on the biochar surface, mediating the electrostatic interactions with the sulfonate groups of dye molecules.[56] Four further concurrent mechanisms – hydrophobic interactions between the biochar surface and aromatic rings of the dye, π–π interactions between the electron-rich aromatic complex of the biochar matrix and the electron-deficient aromatic complex of RY176 dye, ion exchange mechanism between the biochar surface (Cl^-, OH^-) and dye molecules ($-SO_3^-$), and H–H bonding between the –OH, –COOH, –C=O groups on the biochar surface and $-SO_3^-$, $-NH_2$, and –N=N- groups present in the dye – enhanced the adsorption process.[105,106] 700BC demonstrated a superlative adsorption capacity of 18.3 mg g^{-1}, attributed to its microporosity and largest specific surface area. Critically, 500BC exhibited a 12.5% decrease in adsorption capacity despite having a 7-fold lower specific surface area. This comparable adsorption capacity resulted from its optimal surface functionality and superior pore structure (mesoporous, 2–50 nm). Meanwhile, the low surface area (3.5 m^2 g^{-1}) of 300BC and the prevalence of –OH and –COOH on the surface potentially suppressed the π–π interactions,[82] resulting in the lowest adsorption capacity with 7.5 mg g^{-1}.

Previous studies have reported that adsorption of anionic dyes onto mineral-rich biochars can lead to the displacement of inherent mineral ions during adsorption. XRD analysis revealed the presence of minerals such as calcite and sylvite, which might have contributed to ion exchange with dye anions.[107] Broadly, pore filling, electrostatic attraction, ion exchange, π–π stacking or π–electron donor–acceptor interactions, hydrogen bonding, van der Waals forces, and hydrophobic interactions collectively governed the adsorption process.

4 Conclusion

This study demonstrated that water hyacinth biochar prepared through a facile carbonization process can effectively eliminate common textile dyes (Reactive Yellow 176) from aqueous solution. The pyrolysis temperature significantly influenced the surface, textural, and chemical properties of the biochar. The specific surface area of the biochar pyrolyzed at 700 °C (211.3 m^2 g^{-1}) increased nearly 59-fold compared to the 300 °C counterpart (3.6 m^2 g^{-1}) and the total pore volume (cm^3 g^{-1}) exhibited an approximately 7-fold enhancement. The adsorption followed the Langmuir isotherm model and the pseudo-second-order kinetics. The IPD model suggested that surface interaction dominated the adsorption process while the pore diffusion was the rate-limiting step. Higher calcination temperature assisted in the development of an aromatic, carbon-rich porous structure, which substantially promoted dye uptake reaching up to 19.68 mg g^{-1}. The negative values of ΔG (−24.71 to −30.42 kJ mol^{-1}), ΔH (−27.59 to −45.73 kJ mol^{-1}), and ΔS (−7.98 to −52.38 J mol^{-1} K^{-1}) confirmed the spontaneous, exothermic, and more ordered nature of the adsorption for all biochars, respectively. The probable adsorption pathways included electrostatic attractions, π–π interactions, ion exchange mechanisms, H–H bonding, and hydrophobic interactions. The results indicate that water hyacinth can be a sustainable and cost-effective bioadsorbent for dye degradation in aquatic environments, particularly when produced at higher calcination temperatures, which demonstrated strong adsorption performance even under near-neutral pH conditions. Future work may focus on surface modification and regeneration potential to further improve reusability and sorption efficiency, which could make it more suitable for practical applications.

Author contributions

Nawshin Farzana: investigation, data curation, formal analysis, methodology, writing – original draft preparation. Rayhan Bin

Masud: writing – review and editing, visualization. Tahzib Rayhan Himadry: investigation, data curation. Md. Shahinoor Islam: conceptualization, funding, project administration, supervision, writing – review and editing.

Conflicts of interest

The authors have no known conflicts of interest.

Data availability

The data used in this research have been presented throughout the manuscript.

Supplementary information (SI): additional experimental details of biochar preparation and pyrolysis setup (Fig. S1) and EDX spectra (Fig. S2). See DOI: https://doi.org/10.1039/d5su00918a.

Acknowledgements

The authors would like to acknowledge the technical support received from the Bangladesh University of Engineering and Technology (BUET) and the financial support received from the Bangladesh Bureau of Educational Information and Statistics (BANBEIS) under the project ID: T20232849.

References

1 A. P. Periyasamy, Recent Advances in the Remediation of Textile-Dye-Containing Wastewater: Prioritizing Human Health and Sustainable Wastewater Treatment, *Sustainability*, 2024, **16**(2), 495, DOI: 10.3390/su16020495.

2 MdM. Islam, K. Mahmud, O. Faruk and S. Billah, Assessment of environmental impacts for textile dyeing industries in Bangladesh, in: *International Conference on Green Technology and Environmental Conservation (GTEC-2011)*, 2011, pp. 173–181, DOI: 10.1109/GTEC.2011.6167665.

3 A. Khatri, M. H. Peerzada, M. Mohsin and M. White, A review on developments in dyeing cotton fabrics with reactive dyes for reducing effluent pollution, *J. Clean. Prod.*, 2015, **87**, 50–57, DOI: 10.1016/j.jclepro.2014.09.017.

4 M. Javaid Mughal, R. Saeed, M. Naeem, *et al.*, Dye fixation and decolourization of vinyl sulphone reactive dyes by using dicyanidiamide fixer in the presence of ferric chloride, *J. Saudi Chem. Soc.*, 2013, **17**(1), 23–28, DOI: 10.1016/j.jscs.2011.02.017.

5 S. Lykidou, E. Gitsouli, V. Daniilidis, E. Vouvoudi and N. F. Nikolaidis, Study on the Dyeing Properties of a Novel Reactive Dye with One Vinylsulfone Reactive Group, on Cotton Substrates, Before and After Its Ultrafiltration Treatment, *Fibers Polym.*, 2023, **24**(11), 3995–4004, DOI: 10.1007/s12221-023-00366-7.

6 M. Ismail, K. Akhtar, M. I. Khan, T. Kamal, M. A. Asiri, J. Seo, S. B. Khan, *et al.*, Pollution, Toxicity and Carcinogenicity of Organic Dyes and their Catalytic Bio-Remediation, *Curr. Pharm. Des.*, 2019, **25**(34), 3645–3663, DOI: 10.2174/1381612825666191021142026.

7 J. Sharma, S. Sharma and V. Soni, Classification and impact of synthetic textile dyes on Aquatic Flora: A review, *Reg. Stud. Mar. Sci.*, 2021, **45**, 101802, DOI: 10.1016/j.rsma.2021.101802.

8 M. D. Khan, A. Singh, M. Z. Khan, S. Tabraiz and J. Sheikh, Current perspectives, recent advancements, and efficiencies of various dye-containing wastewater treatment technologies, *J. Water Proc. Eng.*, 2023, **53**, 103579, DOI: 10.1016/j.jwpe.2023.103579.

9 A. Tkaczyk, K. Mitrowska and A. Posyniak, Synthetic organic dyes as contaminants of the aquatic environment and their implications for ecosystems: A review, *Sci. Total Environ.*, 2020, **717**, 137222, DOI: 10.1016/j.scitotenv.2020.137222.

10 M. Muduli, M. Choudhary, V. Sonpal and S. Ray, Recent advancements and approaches towards dye industries effluent treatment, *Sustain. Water Resour. Manag.*, 2023, **9**(6), 186, DOI: 10.1007/s40899-023-00975-3.

11 V. Katheresan, J. Kansedo and S. Y. Lau, Efficiency of various recent wastewater dye removal methods: A review, *J. Environ. Chem. Eng.*, 2018, **6**(4), 4676–4697, DOI: 10.1016/j.jece.2018.06.060.

12 A. Monroy-Licht, L. Carranza-Lopez, A. C. De la Parra-Guerra and R. Acevedo-Barrios, Unlocking the potential of Eichhornia crassipes for wastewater treatment: phytoremediation of aquatic pollutants, a strategy for advancing Sustainable Development Goal-06 clean water, *Environ. Sci. Pollut. Res.*, 2024, **31**(31), 43561–43582, DOI: 10.1007/s11356-024-33698-9.

13 K. Nahar and S. A. Sunny, Co-Benefits of Eichhornia Crassipes (Water Hyacinth) as Sustainable Biomass for Biofuel Production and Aquatic Ecosystem Phytoremediation, *Fuels*, 2024, **5**(3), 317–333, DOI: 10.3390/fuels5030018.

14 E. S. Khater, A. Bahnasawy, R. Hamouda, A. Sabahy, W. Abbas and O. M. Morsy, Biochar production under different pyrolysis temperatures with different types of agricultural wastes, *Sci. Rep.*, 2024, **14**(1), 2625, DOI: 10.1038/s41598-024-52336-5.

15 R. Muralikrishnan and C. Jodhi, Biodecolorization of Reactive Dyes Using Biochar Derived from Rice Husk (Oryza Sativa): Batch & Isotherm and Kinetic & Desorption Studies, *Int. Trans. J. Eng., Manage.,Appl. Sci. Technol.*, 2021, **12**(8), 1–15.

16 A. Bobbili, S. R. G. GVR and R. Gokulan, Biodecolorization of Remazol Black B using Biochar produced from Coconut Shell: Batch, Desorption, Isotherm and Kinetic Studies, *Global NEST J.*, 2023, **25**(1), 57–65.

17 https://ijppr.humanjournals.com/wp-content/uploads/2023/07/30.Manisha-Chaudhari.pdf, Accessed February 27, 2026.

18 K. Vijayaraghavan and T. Ashokkumar, Characterization and evaluation of reactive dye adsorption onto Biochar Derived from Turbinaria conoides Biomass, *Environ. Prog. Sustain. Energy*, 2019, **38**(4), 13143, DOI: 10.1002/ep.13143.

19 H. A. Alharbi, B. H. Hameed, K. D. Alotaibi, S. S. Al-Oud and A. S. Al-Modaihsh, Recent methods in the production of activated carbon from date palm residues for the adsorption of textile dyes: A review, *Front. Environ. Sci.*, 2022, **10**, 996953, DOI: 10.3389/fenvs.2022.996953.

20 G. T. Tran, T. T. T. Nguyen, D. T. D. Nguyen, D. H. Nguyen, D. T. C. Nguyen and T. V. Tran, Conversion of invasive plant species (Bidens pilosa L.) into bioadsorbents for simultaneous removal of ciprofloxacin antibiotic and crystal violet dye, *Biomass Convers. Biorefin.*, 2025, **15**(17), 24299–24311, DOI: 10.1007/s13399-024-06082-3.

21 R. T. Kapoor, M. Rafatullah, M. R. Siddiqui, M. A. Khan and M. Sillanpää, Removal of Reactive Black 5 *Dye* by Banana Peel Biochar and Evaluation of Its Phytotoxicity on Tomato, *Sustainability*, 2022, **14**(7), 4176, DOI: 10.3390/su14074176.

22 R. Muralikrishnan and C. Jodhi, Biodecolorization of Reactive Orange 16 using biochar produced from groundnut shell (Arachis hypogaea): batch, isotherm, kinetic, and regeneration studies, *Biomass Convers. Biorefin.*, 2023, **13**(10), 8891–8902, DOI: 10.1007/s13399-021-01710-8.

23 T. Chakraborty, G. Ghosh, M. Akter, K. Audhikary, Md Islam, P. Ghosh, S. Zaman, A. Habib and A. H. M. E. Kabir, Biosorption of Reactive Red 120 Dye from Aqueous Solutions by using Mahagoni (Swietenia mahagoni) Wood and Bark Charcoal: Equilibrium, and Kinetic Studies, *Pollution*, 2021, 7(4), 905–921, DOI: 10.22059/POLL.2021.325135.1110.

24 A. Tomczyk, Z. Sokołowska and P. Boguta, Biochar physicochemical properties: pyrolysis temperature and feedstock kind effects, *Rev. Environ. Sci. Biotechnol.*, 2020, **19**(1), 191–215, DOI: 10.1007/s11157-020-09523-3.

25 Md S. Islam, J.-H. Kwak, C. Nzediegwu, S. Wang, K. Palansuriya, E. E. Kwon, M. Anne Naeth, M. G. El-Din, Y. S. Ok and S. X. Chang, _Biochar heavy metal removal in aqueous solution depends on feedstock type and pyrolysis purging gas, *Environ. Pollut.*, 2021, **281**, 117094, DOI: 10.1016/j.envpol.2021.117094.

26 T. A. Aragaw and F. M. Bogale, Biomass-Based Adsorbents for Removal of Dyes From Wastewater: A Review, *Front. Environ. Sci.*, 2021, **9**, 764958, DOI: 10.3389/fenvs.2021.764958.

27 A. K. Sakhiya, A. Anand and P. Kaushal, Production, activation, and applications of biochar in recent times, *Biochar*, 2020, **2**(3), 253–285, DOI: 10.1007/s42773-020-00047-1.

28 ASTM D2867, Moisture in Activated Carbon | PDF | Chemistry | Nature. Scribd, Accessed February 27, 2026, https://www.scribd.com/document/503207133/Moisture-D2867-04.

29 M. S. Islam, J. H. Kwak, C. Nzediegwu, *et al.*, Biochar heavy metal removal in aqueous solution depends on feedstock type and pyrolysis purging gas, *Environ. Pollut.*, 2021, **281**, 117094, DOI: 10.1016/j.envpol.2021.117094.

30 J. Qu, S. Wang, L. Jin, *et al.*, Magnetic porous biochar with high specific surface area derived from microwave-assisted hydrothermal and pyrolysis treatments of water hyacinth for Cr(VI) and tetracycline adsorption from water, *Bioresour. Technol.*, 2021, **340**, 125692, DOI: 10.1016/j.biortech.2021.125692.

31 K. Y. Foo and B. H. Hameed, Insights into the modeling of adsorption isotherm systems, *Chem. Eng. J.*, 2010, **156**(1), 2–10, DOI: 10.1016/j.cej.2009.09.013.

32 P. Ganguly, R. Sarkhel and P. Das, Synthesis of pyrolyzed biochar and its application for dye removal: Batch, kinetic and isotherm with linear and non-linear mathematical analysis, *Surf. Interfaces*, 2020, **20**, 100616, DOI: 10.1016/j.surfin.2020.100616.

33 T. Tatarchuk, M. Myslin, I. Mironyuk, *et al.*, Synthesis, morphology, crystallite size and adsorption properties of nanostructured Mg–Zn ferrites with enhanced porous structure, *J. Alloys Compd.*, 2020, **819**, 152945, DOI: 10.1016/j.jallcom.2019.152945.

34 A. K. Behera, K. P. Shadangi and P. K. Sarangi, Efficient removal of Rhodamine B dye using biochar as an adsorbent: Study the performance, kinetics, thermodynamics, adsorption isotherms and its reusability, *Chemosphere*, 2024, **354**, 141702, DOI: 10.1016/j.chemosphere.2024.141702.

35 A. Abuabara, C. Diaz-Uribe, W. Vallejo, F. Duran and E. Mosquera-Vargas, Kinetic and Thermodynamic Study of Cationic Dye Removal Using Activated Biochar Synthesized from *Prosopis juliflora* Waste, *ChemEngineering*, 2025, **9**(3), 64, DOI: 10.3390/chemengineering9030064.

36 E. C. Lima, A. Hosseini-Bandegharaei, J. C. Moreno-Piraján and I. Anastopoulos, A critical review of the estimation of the thermodynamic parameters on adsorption equilibria. Wrong use of equilibrium constant in the Van't Hoof equation for calculation of thermodynamic parameters of adsorption, *J. Mol. Liq.*, 2019, **273**, 425–434, DOI: 10.1016/j.molliq.2018.10.048.

37 R. Chang and J. Thoman, *Physical Chemistry for the Chemical Sciences*, Royal Society of Chemistry, 2014, Accessed February 27, 2026, https://books.rsc.org/books/monograph/2168/Physical-Chemistry-for-the-Chemical-Sciences.

38 A. G. Gezahegn, Y. Selassie, G. Agegnehu, *et al.*, Pyrolysis temperature changes the physicochemical characteristics of water hyacinth-based biochar as a potential soil amendment, *Biomass Convers. Biorefin.*, 2025, **15**(3), 3737–3752, DOI: 10.1007/s13399-024-05338-2.

39 Y. Li, R. Gupta, Q. Zhang and S. You, Review of biochar production via crop residue pyrolysis: Development and perspectives, *Bioresour. Technol.*, 2023, **369**, 128423, DOI: 10.1016/j.biortech.2022.128423.

40 J. Zhang, J. Liu and R. Liu, Effects of pyrolysis temperature and heating time on biochar obtained from the pyrolysis of straw and lignosulfonate, *Bioresour. Technol.*, 2015, **176**, 288–291, DOI: 10.1016/j.biortech.2014.11.011.

41 I. C. Akendo, L. O. Gumbe and A. N. Gitau, Dewatering and Drying Characteristics of Water Hyacinth (Eichhornia

Crassipes) Petiole. Part II. Drying Characteristics, *Agric. Eng. Int.: CIGR J.*, 2008, **10**, 1–11.

42 S. Liu, S. Peng, B. Zhang, *et al.*, Effects of biochar pyrolysis temperature on thermal properties of polyethylene glycol/biochar composites as shape-stable biocomposite phase change materials, *RSC Adv.*, 2022, **12**(16), 9587–9598, DOI: 10.1039/D1RA09167K.

43 P. Srivatsav, B. S. Bhargav, V. Shanmugasundaram, J. Arun, K. P. Gopinath and A. Bhatnagar, Biochar as an Eco-Friendly and Economical Adsorbent for the Removal of Colorants (Dyes) from Aqueous Environment: A Review, *Water*, 2020, **12**(12), 3561, DOI: 10.3390/w12123561.

44 R. M. Silverstein, F. X. Webster and D. J. Kiemle, *Spectrometric Identification of Organic Compounds*, John Wiley & Sons, Inc., References - Scientific Research Publishing, Hoboken, 7th edn, 2005, Accessed February 27, 2026, https://www.scirp.org/reference/referencespapers?referenceid=3206455.

45 M. N. Siddiquee and A. De Klerk, Hydrocarbon addition reactions during low-temperature autoxidation of oilsands bitumen, *Energy Fuels*, 2014, **28**(11), 6848–6859, DOI: 10.1021/ef501694s.

46 L. S. Mohamed, M. M. Hossain and M. N. Siddiquee, Investigation of controlled autoxidation of HVGO to produce carbon fibres precursors: Role of oxygen availability and mixing, *Chem. Eng. Res. Des.*, 2024, **205**, 433–442, DOI: 10.1016/j.cherd.2024.04.011.

47 A. Ray, A. Banarjee and A. Dubey, Characterization of Biochars from Various Agricultural By-Products Using FTIR Spectroscopy, SEM focused with image Processing, *Int. J. Agric. Environ. Biotechnol.*, 2020, **13**(4), 423–430, DOI: 10.30954/0974-1712.04.2020.6.

48 Y. Liu, Z. He and M. Uchimiya, Comparison of Biochar Formation from Various Agricultural By-Products Using FTIR Spectroscopy, *Mod. Appl. Sci.*, 2015, **9**(4), 246, DOI: 10.5539/mas.v9n4p246.

49 M. Mujtaba, L. Fernandes Fraceto, M. Fazeli, *et al.*, Lignocellulosic biomass from agricultural waste to the circular economy: *a review with focus on biofuels, biocomposites and bioplastics*, *J. Clean. Prod.*, 2023, **402**, 136815, DOI: 10.1016/j.jclepro.2023.136815.

50 M. Rojo, D. Álvarez-Muñoz, A. Dománico, *et al.*, Human pharmaceuticals in three major fish species from the Uruguay River (South America) with different feeding habits, *Environ. Pollut.*, 2019, **252**, 146–154, DOI: 10.1016/j.envpol.2019.05.099.

51 B. Bushra and N. Remya, Biochar from pyrolysis of rice husk biomass—characteristics, modification and environmental application, *Biomass Convers. Biorefin.*, 2024, **14**(5), 5759–5770, DOI: 10.1007/s13399-020-01092-3.

52 W. Barszcz, M. Łożyńska and J. Molenda, Impact of pyrolysis process conditions on the structure of biochar obtained from apple waste, *Sci. Rep.*, 2024, **14**(1), 10501, DOI: 10.1038/s41598-024-61394-8.

53 Z. Chang, L. Tian, J. Zhang and D. Zhou, Comparative study on the relative significance of low-/high-condensation aromatic moieties in biochar to organic contaminant sorption, *Ecotoxicol. Environ. Saf.*, 2022, **238**, 113598, DOI: 10.1016/j.ecoenv.2022.113598.

54 P. Conte, R. Bertani, P. Sgarbossa, P. Bambina, H.-P. Schmidt, R. Raga, G. Lo Papa, D. F. Chillura Martino and P. Lo Meo, Recent Developments in Understanding Biochar's Physical–Chemistry, *Agronomy*, 2021, **11**(4), 615, DOI: 10.3390/agronomy11040615.

55 J. Lehmann and S. Joseph, *Biochar for Environmental Management: an Introduction. Biochar for Environmental Management. Science and Technology*, Earthscan Publishers Ltd, 2009.

56 A. L. Srivastav, L. Rani, P. Sharda, A. Patel, N. Patel and V. K. Chaudhary, Sustainable biochar adsorbents for dye removal from water: present state of art and future directions, *Adsorption*, 2024, **30**(7), 1791–1804, DOI: 10.1007/s10450-024-00522-2.

57 A. D. French and M. Santiago Cintrón, Cellulose polymorphy, crystallite size, and the Segal Crystallinity Index, *Cellulose*, 2013, **20**(1), 583–588, DOI: 10.1007/s10570-012-9833-y.

58 H. H. Muigai, U. Bordoloi, R. Hussain, K. Ravi, V. S. Moholkar and P. Kalita, A comparative study on synthesis and characterization of biochars derived from lignocellulosic biomass for their candidacy in agronomy and energy applications, *Int. J. Energy Res.*, 2021, **45**(3), 4765–4781, DOI: 10.1002/er.6092.

59 M. Keiluweit, P. S. Nico, M. G. Johnson and M. Kleber, *Environ. Sci. Technol.*, 2010, **44**(4), 1247–1253DOI, DOI: 10.1021/es9031419.

60 S. A. El-Sayed, T. M. Khass and M. E. Mostafa, Thermal degradation behaviour and chemical kinetic characteristics of biomass pyrolysis using TG/DTG/DTA techniques, *Biomass Convers. Biorefin.*, 2024, **14**(15), 17779–17803, DOI: 10.1007/s13399-023-03926-2.

61 C. B. Peres, A. H. Rosa and L. C. de Morais, CO2 adsorption of bagasse waste feedstock using thermogravimetric analyses, *J. Therm. Anal. Calorim.*, 2022, **147**(10), 5973–5984, DOI: 10.1007/s10973-021-10949-2.

62 X. Zou, P. Debiagi, M. A. Amjed, M. Zhai and T. Faravelli, Impact of high-temperature biomass pyrolysis on biochar formation and composition, *J. Anal. Appl. Pyrolysis*, 2024, **179**, 106463, DOI: 10.1016/j.jaap.2024.106463.

63 L. C. Morais, A. A. D. Maia, M. E. G. Guandique and A. H. Rosa, Pyrolysis and combustion of sugarcane bagasse, *J. Therm. Anal. Calorim.*, 2017, **129**(3), 1813–1822, DOI: 10.1007/s10973-017-6329-x.

64 K. Skic, A. Adamczuk, A. Gryta, P. Boguta, T. Tóth and G. Jozefaciuk, Surface areas and adsorption energies of biochars estimated from nitrogen and water vapour adsorption isotherms, *Sci. Rep.*, 2024, **14**(1), 30362, DOI: 10.1038/s41598-024-81030-9.

65 E. Santoso, R. Ediati, Y. Kusumawati, H. Bahruji, D. O. Sulistiono and D. Prasetyoko, Review on recent advances of carbon based adsorbent for methylene blue removal from waste water, *Mater. Today Chem.*, 2020, **16**, 100233, DOI: 10.1016/j.mtchem.2019.100233.

66 T. J. Jiang, H. M. Morgan, W. T. Tsai, H. Chien, T. B. Yen and Y. R. Lee, Thermochemical Conversion of Biomass into Biochar: Enhancing Adsorption Kinetics and Pore Properties for Environmental Sustainability, *Sustainability*, 2024, **16**(15), 6623, DOI: 10.3390/su16156623.

67 M. T. Carneiro, A. Morais, A. L. F. de Carvalho Melo, *et al.*, Biochar Derived from Water Hyacinth Biomass Chemically Activated for Dye Removal in Aqueous Solution, *Sustainability*, 2023, **15**(19), 14578, DOI: 10.3390/su151914578.

68 I. G. Edeh, O. Masek and F. Fusseis, 4D structural changes and pore network model of biomass during pyrolysis, *Sci. Rep.*, 2023, **13**(1), 22863, DOI: 10.1038/s41598-023-49919-z.

69 X. Zhang, B. Zhao, H. Liu, Y. Zhao and L. Li, Effects of pyrolysis temperature on biochar's characteristics and speciation and environmental risks of heavy metals in sewage sludge biochars, *Environ. Technol. Innov.*, 2022, **26**, 102288, DOI: 10.1016/j.eti.2022.102288.

70 C. Liu, J. Ye, Y. Lin, *et al.*, Removal of Cadmium (II) using water hyacinth (*Eichhornia crassipes)* biochar alginate beads in aqueous solutions, *Environ. Pollut.*, 2020, **264**, 114785, DOI: 10.1016/j.envpol.2020.114785.

71 F. Li, K. Shen, X. Long, *et al.*, Preparation and Characterization of Biochars from Eichornia crassipes for Cadmium Removal in Aqueous Solutions, *PLoS One*, 2016, **11**(2), e0148132, DOI: 10.1371/journal.pone.0148132.

72 A. T. Irewale, E. E. Elemike, A. M. Shaik, C. O. Dimkpa and E. E. Oguzie, Theoretical and experimental insights into BET surface area and pore analysis of water hyacinth biochar: Prospects for efficient bio-nanofertilizer development, *MRS Adv.*, 2025, **10**(9), 1029–1035, DOI: 10.1557/s43580-025-01248-1.

73 J. Jabar, M. Adebayo, A. Owokotomo, Y. Odusote and M. Yılmaz, Synthesis of high surface area mesoporous ZnCl 2 -activated cocoa (Theobroma cacao L) leaves biochar derived via pyrolysis for crystal violet dye removal, *Heliyon*, 2022, **8**, e10873, DOI: 10.1016/j.heliyon.2022.e10873.

74 B. Handiso, T. Pääkkönen and B. P. Wilson, Effect of pyrolysis temperature on the physical and chemical characteristics of pine wood biochar, *Waste Manag. Bull.*, 2024, **2**(4), 281–287, DOI: 10.1016/j.wmb.2024.11.008.

75 A. Palamanit, P. Khongphakdi, Y. Tirawanichakul and N. Phusunti, Investigation of yields and qualities of pyrolysis products obtained from oil palm biomass using an agitated bed pyrolysis reactor, *Biofuel Res. J.*, 2019, **6**(4), 1065–1079.

76 Z. Chowdhury, M. Karim, M. A. Ashraf and K. Khalisanni, Influence of Carbonization Temperature on Physicochemical Properties of Biochar derived from Slow Pyrolysis of Durian Wood (Durio zibethinus) Sawdust, *Bioresources*, 2016, **11**, 3356–3372.

77 K. H. Kim, J. Y. Kim, T. S. Cho and J. W. Choi, Influence of pyrolysis temperature on physicochemical properties of biochar obtained from the fast pyrolysis of pitch pine (*Pinus rigida*), *Bioresour. Technol.*, 2012, **118**, 158–162, DOI: 10.1016/j.biortech.2012.04.094.

78 M. Burachevskaya, T. Minkina, T. Bauer, *et al.*, Fabrication of biochar derived from different types of feedstocks as an efficient adsorbent for soil heavy metal removal, *Sci. Rep.*, 2023, **13**(1), 2020, DOI: 10.1038/s41598-023-27638-9.

79 E. Avramiotis, Z. Frontistis, I. D. Manariotis, J. Vakros and D. Mantzavinos, On the Performance of a Sustainable Rice Husk Biochar for the Activation of Persulfate and the Degradation of Antibiotics, *Catalysts*, 2021, **11**(11), 1303, DOI: 10.3390/catal11111303.

80 M. E. Saleh, A. A. El-Refaey and A. H. Mahmoud, Effectiveness of sunflower seed husk biochar for removing copper ions from wastewater: a comparative study, *Soil Water Res.*, 2016, **11**(1), 53–63.

81 C. F. Chiu and Z. D. Huang, Microbial Methane Oxidation and Gas Adsorption Capacities of Biochar-Modified Soils, *Int. J. Geosynth Ground Eng.*, 2020, **6**(2), 24, DOI: 10.1007/s40891-020-00202-5.

82 M. Singh, M. Ahsan, V. Pandey, *et al.*, Comparative assessment for removal of anionic dye from water by different waste-derived biochar vis a vis reusability of generated sludge, *Biochar*, 2022, **4**(1), 13, DOI: 10.1007/s42773-022-00140-7.

83 J. H. Yuan, R. K. Xu and H. Zhang, The forms of alkalis in the biochar produced from crop residues at different temperatures, *Bioresour. Technol.*, 2011, **102**(3), 3488–3497, DOI: 10.1016/j.biortech.2010.11.018.

84 D. Angın, Effect of pyrolysis temperature and heating rate on biochar obtained from pyrolysis of safflower seed press cake, *Bioresour. Technol.*, 2013, **128**, 593–597, DOI: 10.1016/j.biortech.2012.10.150.

85 D. M. Lewis, P. J. Broadbent, C. M. Carr and W. D. He, Investigation into the reaction of reactive dyes with carboxylate salts and the application of carboxylate-modified reactive dyes to cotton, *Color. Technol.*, 2022, **138**(1), 58–70, DOI: 10.1111/cote.12571.

86 Y. Shen, S. Han, Q. Xu, *et al.*, Optimizing degradation of Reactive Yellow 176 by dielectric barrier discharge plasma combined with TiO2 nano-particles prepared using response surface methodology, *J. Taiwan Inst. Chem. Eng.*, 2016, **60**, 302–312, DOI: 10.1016/j.jtice.2015.10.018.

87 A. Aichour, H. Zaghouane-Boudiaf and H. D. Khodja, Highly removal of anionic dye from aqueous medium using a promising biochar derived from date palm petioles: Characterization, adsorption properties and reuse studies, *Arab. J. Chem.*, 2022, **15**(1), 103542, DOI: 10.1016/j.arabjc.2021.103542.

88 P. T. Le, H. T. Bui, D. N. Le, *et al.*, Preparation and Characterization of Biochar Derived from Agricultural By-Products for Dye Removal, *Adsorpt. Sci. Technol.*, 2021, **2021**, 9161904, DOI: 10.1155/2021/9161904.

89 N. U. M. Nizam, M. M. Hanafiah, E. Mahmoudi, A. A. Halim and A. W. Mohammad, The removal of anionic and cationic dyes from an aqueous solution using biomass-based activated carbon, *Sci. Rep.*, 2021, **11**(1), 8623, DOI: 10.1038/s41598-021-88084-z.

90 M. Abdu, S. Babaee, A. Worku, T. A. M. Msagati and J. F. Nure, The development of Giant reed biochar for

adsorption of Basic Blue 41 and Eriochrome Black T. azo dyes from wastewater, *Sci. Rep.*, 2024, **14**(1), 18320, DOI: 10.1038/s41598-024-67997-5.

91 M. Amin and P. Chetpattananondh, Biochar from extracted marine *Chlorella* sp. residue for high efficiency adsorption with ultrasonication to remove Cr(VI), Zn(II) and Ni(II), *Bioresour. Technol.*, 2019, **289**, 121578, DOI: 10.1016/j.biortech.2019.121578.

92 L. Goswami, A. Kushwaha, S. R. Kafle and B.-S. Kim, Surface Modification of Biochar for Dye Removal from Wastewater, *Catalysts*, 2022, **12**(8), 817, DOI: 10.3390/catal12080817.

93 M. Wei, X. Duan, W. Zhou, K. Huang, Y. Chen and J. Tie, Enhanced Adsorption of Two Reactive Dyes onto Al-Based Waterworks Sludge Modified by Calcination, *Pol. J. Environ. Stud.*, 2023, **32**(3), 2373–2381.

94 R. T. Kapoor, M. Rafatullah, M. R. Siddiqui, M. A. Khan and M. Sillanpää, Removal of Reactive Black 5 Dye by Banana Peel Biochar and Evaluation of Its Phytotoxicity on Tomato, *Sustainability*, 2022, **14**(7), 4176, DOI: 10.3390/su14074176.

95 I. N. Sukarta, I. W. B. Suyasa, I. G. Mahardika, I. E. Suprihatin and I. D. K. Sastrawidana, Innovation of Remazol yellow FG dye adsorption using biochar from coffee fruit shell waste, *J. Econ. Eng.*, 2025, **26**(1), 273–285.

96 V. Gajendiran, P. Deivasigamani, S. Sivamani and S. Banerjee, Biochar from *Manihot esculenta* stalk as potential adsorbent for removal of Reactive Yellow dye, *Desalination Water Treat.*, 2024, **317**, 100120, DOI: 10.1016/j.dwt.2024.100120.

97 Y. S. Ho and G. McKay, Pseudo-second order model for sorption processes, *Process Biochem.*, 1999, **34**(5), 451–465, DOI: 10.1016/S0032-9592(98)00112-5.

98 S. Garg, N. P. Rumjit, P. Arora and S. Ahmed, Biochar-based solutions for sustainable dye treatment and agricultural waste management, *J. Mater. Cycles Waste Manag.*, 2025, **27**(3), 1283–1301, DOI: 10.1007/s10163-025-02201-y.

99 R. Chavan, R. Patil, and A. D. Chougale, *Efficient Dye Removal Strategies: Exploring the Role of Biochar*, ChemSci Advances, 2024.

100 F. Lian and B. Xing, Black Carbon (Biochar) In Water/Soil Environments: Molecular Structure, Sorption, Stability, and Potential Risk, *Environ. Sci. Technol.*, 2017, **51**(23), 13517–13532, DOI: 10.1021/acs.est.7b02528.

101 H. N. Tran, S. J. You, A. Hosseini-Bandegharaei and H. P. Chao, Mistakes and inconsistencies regarding adsorption of contaminants from aqueous solutions: A critical review, *Water Res.*, 2017, **120**, 88–116, DOI: 10.1016/j.watres.2017.04.014.

102 X. Li, Y. Wang, C. Chen, C. Tian, X. Yu, J. Liu, Q. Li and S. Wang, Sustainable biochar derived from waste lotus seedpod for efficient adsorption of residual carbamate pesticides, *Heliyon*, 2025, **11**(5), e42741, DOI: 10.1016/j.heliyon.2025.e42741.

103 S. Senapati, J. Giri, L. Mallick, *et al.*, Rapid adsorption of industrial cationic dye pollutant using base-activated rice straw biochar: performance, isotherm, kinetic and thermodynamic evaluation, *Discov. Sustain.*, 2025, **6**(1), 46, DOI: 10.1007/s43621-025-00835-4.

104 A. Erdem Yayayürük, N. Çankaya and O. Yayayürük, Advancing eco-friendly adsorption: a sustainable approach for rapid and efficient methylene blue removal, *Polym. Bull.*, 2025, **82**(8), 3207–3223, DOI: 10.1007/s00289-025-05662-1.

105 X. Tan, Y. Liu, G. Zeng, *et al.*, Application of biochar for the removal of pollutants from aqueous solutions, *Chemosphere*, 2015, **125**, 70–85, DOI: 10.1016/j.chemosphere.2014.12.058.

106 D. S. S and V. Vishwakarma, Recovery and recycle of wastewater contaminated with heavy metals using adsorbents incorporated from waste resources and nanomaterials-A review, *Chemosphere*, 2021, **273**, 129677, DOI: 10.1016/j.chemosphere.2021.129677.

107 G. Ravenni, Z. Sárossy, S. Sanna, J. Ahrenfeldt and U. B. Henriksen, Residual gasification char applied to tar reforming in a pilot-scale gasifier: Performance and evolution of char properties for perspective cascade uses, *Fuel Process. Technol.*, 2020, **210**, 106546, DOI: 10.1016/j.fuproc.2020.106546.